An objective climatology of Polar Lows: structure and forcing mechanisms

Sebastiaan Crezee

August 30, 2013

Supervisors:
dr. A.J. van Delden (Utrecht University, NL)
dr. T. Spengler (University of Bergen, NO)

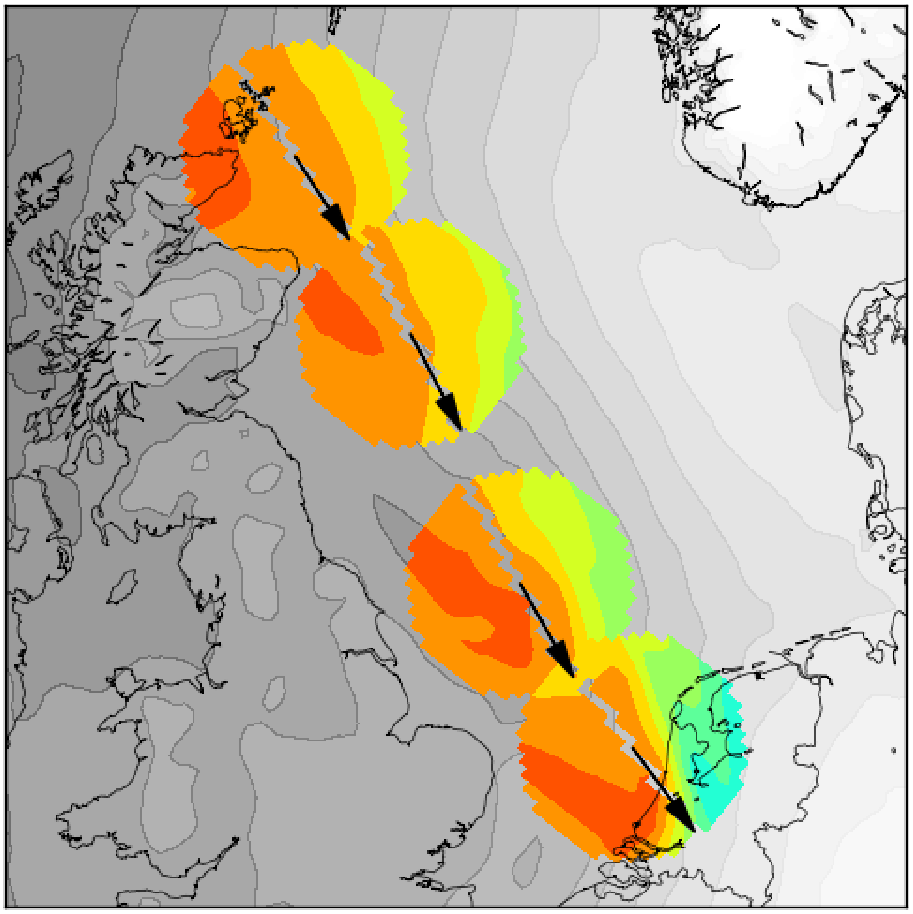

Abstract

Polar lows are strong mesoscale cyclones occurring during outbreaks of cold arctic air over relatively warm seas. A long-term objective polar low climatology is constructed by identifying and tracking cyclones in a high-resolution dynamical downscaling of ERA-40 covering a part of the North Atlantic, the North Sea and the Nordic Seas. Regions of high polar low occurrence are found to the south of Iceland and in the eastern Norwegian Sea and Barents Sea. In these regions on average 2 polar lows per year can be found within a radius of 200 km.

The polar low climatology (2000 polar low tracks) is used to study polar low structure and forcing mechanisms. Polar low structure is analyzed by calculating for each polar low two different parameters based on the geopotential height fields surrounding the cyclone: thermal asymmetry (frontal / non-frontal) and thermal core (warm / cold). Plotting these parameters against each other shows a wide spectrum with the very symmetric hurricane-like polar lows on the one end of the spectrum and the asymmetric cold-core structures on the other side of the spectrum. It is shown that most polar lows (70%) are characterized by a shallow warm core and occur in a forward-shear environment with the thermal wind aligned with polar low motion.

Warm core polar lows show a larger pressure-drop before their mature stage than systems with a colder core, which is consistent with existing theories. Also mean values of surface heat fluxes are found to be strongest for the warm-core systems.

The large number of polar lows allows for investigating regional variations in the forcing parameters. We find that polar lows in the northern Norwegian Sea are characterized by stronger low-level baroclinicity and a larger air stability than polar lows more to the south. For future studies it would be interesting to include the roles of latent heat release and upper-level disturbances, by using potential vorticity diagnostics.

Front page illustration: Track of a polar low making landfall in The Netherlands on 2 january 1979. Contours show 1000-850 hPa geopotential thickness fields in a radius of 120 km around the polar low, it is one of the parameters used to study PL structure.

Contents

1 Introduction

> A polar low is a small, but fairly intense maritime cyclone that forms poleward of the main baroclinic zone (the polar front or other major baroclinic zone). The horizontal scale of the polar low is approximately between 200 and 1000 kilometres and surface winds near or above gale force.

This is the definition of a polar low according to Rasmussen and Turner (2003). With the strong winds and snowfall accompanying these maritime cyclones they form a major threat to human activity in off-shore and coastal areas. They occur during the winter half-year during cold air outbreaks over relatively warm seas. Due to their small scales and the scarcity of observations over sea, polar lows are a major challenge for numerical weather prediction. In order to improve predictability of these systems it is important to fully understand the physical mechanism describing their formation, intensification and maintenance. Through a combined effort of observations and numerical simulations during the past half century, the basic theory for polar lows has been developed. Many authors agree that polar lows develop from a finite-amplitude disturbance which can either be an upper-level PV anomaly or a low-level baroclinic zone. After some stage of initial development diabatic processes like latent heating in moist convection and surface heat fluxes explain the intensification and maintenance of the polar low. Some authors (e.g. Emanuel and Rotunno (1989)) have emphasized the similarity of polar lows to tropical cyclones as being very symmetric cyclones possessing a warm core. Others (e.g. Reed and Duncan (1987)) stressed on the importance of baroclinicity for the development of polar lows, which is directly related to an asymmetric thermal structure. In later studies (e.g. Businger and Reed (1989)) it was recognized that there exists a wide spectrum of polar lows ranging from the symmetric ”Arctic hurricanes” on the one end of the spectrum to the very asymmetric systems characterized by a comma-shaped cloud shield on the other end, with a large number of polar lows being a mixture between these two. This wide range of polar lows and the similarity to tropical cyclones raised the idea to capture this spectrum in a phase-space based on thermal wind balance, which was originally developed by Hart (2003) to study tropical and extra-tropical cyclones. Besides revealing the polar low spectrum in terms of thermal structure the phase-space can also be used for exploring different forcing mechanisms. Before the phase-space can be constructed, a polar low climatology has to be constructed. Summarizing the above, the following research objectives can be identified. (1) Obtain a long-term objective polar low climatology. (2) Use this climatology to investigate the structure of the polar lows in terms of their thermal asymmetry and thermal core structure. (3) Study the relation between thermal structure and the strength of different forcing mechanisms (baroclinicity, surface heat fluxes and vertical instability) and investigate any regional variations in these forcing mechanisms.

In order to resolve the small-scale polar lows, a high-resolution (10-11 km in the horizontal directions) dynamical downscaling of ERA-40 from 1970-2012 is used. The domain covers the northeast Atlantic Ocean, North Sea and Nordic Seas. The climatology is constructed by applying a tracking algorithm on minima in the mean sea-level pressure and then selecting the polar low tracks based on an objective identification. The structure and forcing mechanisms of the polar lows are studied by defining for each polar low suitable parameters which can be calculated from the available meteorological fields.

Section 2 gives a chronological overview of polar low research followed by some polar low climatology. In section 3 we give a brief description of the model used in this study. It is followed by a case-study in section 4 where the model is compared to dropsonde observations in a polar low. In section 5 the methods - the cyclone tracking algorithm, the polar low identification method and the diagnostics - are presented. The results are presented in section 6 followed by a discussion in section 7 and finally the conclusion is presented together with a future outlook.

2 Background

First a chronological overview of the development of the main theories on polar low formation is presented in section 2.1, followed by a brief overview of polar low climatologies in section 2.2.

2.1 Historical overview

The famous Norwegian meteorologist Vilhelm Bjerkness already mentioned one of the reasons for the extreme weather occurring in the northern parts of Norway during winter times in a newspaper article in 1904:

> ”The northernmost part of Norway in winter is one of the stormiest locations on Earth, and the terrible accidents that occur from time to time, when large parts of the fishing fleet with crew and tools are lost, are only too well known. A look at the climatological conditions shows that the reason for the frequency of the storms is that the mean temperature in January by the outermost Lofoten Islands is 27 degrees Celsius higher than the mean for the same latitude around the globe. This is the effect of the warm waters of the Gulf Stream. At the same time a Siberian winter cold reigns on the Finnmark plateau. Nature has, in other words, put an immense steam kettle side by side with an immense condenser. This steam engine must always work, and that is what it does, with great, irregular strokes.”

Without explicitly mentioning polar lows, Vilhelm Bjerkness was aware that the strong temperature contrasts between the sea and the surrounding land gave rise to severe winter weather.

While the main theories on extra-tropical cyclones were developed by Bjerkness and his scholars during the 1920s, the polar low research started only from the 1960s. In the next paragraphs a chronological overview of the theories on polar low development will be given.

Early work Harley (1960) presented the first case study of a polar low. Harrold and Browning (1969) analyzed a polar low which crossed Great Britain by using Doppler radar and showed that this polar low was not driven by small-scale convective overturning, but instead by slantwise convection related to a baroclinic zone. Mansfield (1974) proposed the first quantitative theory of polar low formation by using a dry baroclinic model and neglecting surface friction. For a shallow disturbance with a depth of about 1.6 km this theory gives e-folding time-scales of about 1 day for the fastest growing mode corresponding to a wavelength of about 500 km. This is in agreement with observations. Duncan (1977) found that baroclinicity is essential for polar low formation and also that the vertical wind shear has to be parallel to the flow at the steering-level. Later Duncan (1978) showed that reverse-shear conditions - in which the thermal wind is anti-parallel to the steering-level flow - could be favourable as well. Several of the polar lows studied in later years were indeed reverse-shear polar lows. Reed and Duncan (1987) derived a linear quasi-geostrophic, dry baroclinic model and showed that the characteristics of an observed train of polar lows developing in a reversed shear flow were in agreement with this model. In the classical situation - common for extra-tropical cyclones - the cyclone develops in a situation with the warm air to the right of the steering-level flow, thus creating a positive vertical windshear with winds increasing with height. In the reverse-shear situation the warm air is to the left of the flow at the steering-level leading to a negative thermal wind and thus with strongest windspeeds near the surface and upper-level winds sometimes nearly stagnant, also there is a forward tilt of the disturbance in the vertical. Businger and Reed (1989) showed that in the reverse-shear case there is warm advection and rising motion behind the disturbance, while cold advection and sinking motion dominate downstream of the disturbance. This pattern is a direct thermal circulation in which available potential energy (baroclinicity) is converted into kinetic energy. Several authors argued that baroclinic instability alone did not account for the rapidity of polar low intensification and that thus other processes are important as well (e.g. Reed and Duncan (1987)). The hypothesis that diabatic processes contribute significantly to the intensification and maintenance of polar lows was widely supported. However, which diabatic processes were most relevant has been discussed for a long period of time.

The CISK and WISHE controversary Rasmussen (1979) and Rasmussen (1981) proposed CISK or Convective Instability of the Second Kind as the main mechanism for intensification of polar lows in the North Atlantic. The CISK theory was initially developed to describe hurricane intensification. Although the atmosphere in high latitudes is usually much more stable than in the tropics, it was argued that during outbreaks of cold air over the relatively warm sea, the atmosphere can become conditionally unstable. Destabilization of the atmosphere occurs initially through radiation, surface fluxes and other forcing mechanisms, resulting in convection. The CISK theory describes the cooperative intensification of the organized moist convection and the cyclone-scale vortex. Through latent heat release in moist convection the vortex intensifies, this intensification leads to a stronger moisture flux convergence and organization of the convection. The latent heating of the mid and lower troposphere through moist convection gives rise to the typical warm-core structure which is observed in all hurricanes and also in some polar lows. Whether or not CAPE is a pre-requisite for the CISK mechanism has been discussed by several authors (e.g. Linders and Saetra (2010)). Through organization of the convection, cooperative intensification takes place and the vortex spins up by adjustment to gradient wind balance. Since the CISK theory links small-scale processes like moisture convection to the large-scale flow, some kind of closure has to be defined to describe the link between the two. Charney and Eliassen (1964) prescribe a closure in which latent heating is proportional to moisture convergence in the boundary layer, while Ooyama (1964) links the strength of the cumulus convection to the large-scale balanced flow by making the latent heating proportional to the surface friction in the boundary layer. For both approaches an increasing vortex strength leads to increased moisture convergence and surface friction respectively, thereby increasing the cumulus convection.

The opposing theory to CISK was introduced by Emanuel (1986) as air-sea interaction instability theory, and has been renamed wind-induced surface heat exchange (WISHE). The concept for this theory is that tropical cyclones develop entirely by self-induced fluxes of heat and moisture from the sea surface with virtually no contribution from pre-existing CAPE. In this conceptual model the role of the moist convection is solely to redistribute heat acquired from the sea surface, such that the vertical temperature and humidity profile is neutral to slantwise moist convection, consistent with the concept of quasi-equilibrium introduced by Arakawa and Schubert (1974). This means that the ambient environment is conditionally neutral such that any kinetic energy generation is due to the in situ generation of CAPE rather than ambient CAPE. Xu and Emanuel (1989) argue that CISK can not be a working mechanism for tropical cyclones since the atmosphere is not conditionally unstable but rather neutral with respect to moist convection.

The two different theories - CISK and WISHE - have existed in parallel for a longer period of time already. It is hard to distinguish between the two since the relevant processes involved in the theories are all collocated in both space and time during polar low development. This in combination with the limited amount of observations of polar lows makes it hard to distinguish between cause and effect of convection, surface fluxes and frictional convergence.

Emphasis has been put on the question whether or not the atmosphere is unstable with respect to moist convection. This could be measured by means of the Convective Available Potential Energy which expresses the potential buoyant energy for a parcel lifted from the surface along a dry-adiabat to the lifted condensation level and then lifted further along a moist adiabat. It is important to note that both the CISK and the WISHE theory predict the warm-core structure for a polar low, and thus analysis of the polar low structure alone does not provide any information on which mechanism is acting. Further, the two theories do not exclude each other. Authors favouring the CISK theory acknowledge that surface heat fluxes are relevant for maintaining the small CAPE reservoir. On the other hand authors who support the WISHE theory stress that the existence of small CAPE values is not in contradiction with the theory.

Craig and Gray (1996) argue that WISHE can be interpreted as another variant of the CISK theory. Both theories predict a vortex growing from a finite-amplitude disturbance in a balanced flow. It is the closure assumption which makes the WISHE theory different from the CISK theories introduced by Ooyama

(1964) and Charney and Eliassen (1964). The closure for the WISHE theory is the strength of the air-sea interaction in terms of moisture and heat fluxes. Craig and Gray (1996) investigated the validity of the CISK and WISHE theories by means of a convection permitting axi-symmetric numerical model. They showed that vortex intensification is sensitive to the surface heat and moisture transfer coefficients, while it is insensitive to the momentum transfer coefficient. These results show that the rate-limiting process for vortex intensification is the transfer of heat and moisture from the ocean surface to the atmosphere thus in accordance with the WISHE theory.

Recent work Bracegirdle and Gray (2008) investigated the dynamical forcing of polar lows in the Norwegian and Barents seas. They calculated the relative contributions of upper-level and low-level forcings to the mid-level vertical motion. They showed that about thirty percent of the polar lows were dominated by upper-level forcings. The atmospheric conditions associated with this subset of polar lows was found to be consistent with the type-C extra-tropical cyclones in the extended classification scheme of Deveson et al. (2002). This C-type genesis is characterized by strong latent heating which can act as a dynamical surrogate to low-level baroclinicity (Snyder and Lindzen (1991)). Linders and Saetra (2010) calculated CAPE values from dropsonde observations inside and in the environment of polar lows over the Norwegian Sea obtained during the Andøya field campaign (Kristjánsson et al. (2011)). They found relatively low values of CAPE and calculated the time it would take to build up this CAPE from a zero-state by surface fluxes from the ocean. Typical time-scales were on the order of one hour. Also they found that the CAPE was already in the stage of being released. From these two observations they concluded that CAPE has to be seen as a temporary stage in an energy flux rather than a reservoir of energy. Also they state that the sequential view on polar low genesis in which baroclinic instability dominates the early intensification and WISHE takes over in later stages, should be replaced with the two acting together. They suggest that it would be interesting to investigate if surface fluxes will be able to generate baroclinic potential energy at a rate similar to its consumption.

2.2 Climatology

Since the availability of satellite imagery, several authors have compiled climatologies of polar lows. The first known satellite image of a polar low was obtained on the 5th of january 1970 (Lyall (1972)). More than a decade later Wilhelmsen (1985) used satellite imagery, synoptic observations and weather maps to construct a first 10 year climatology of polar lows in the Nordic Seas (see figure 1a).

By making use of numerical reanalysis data attempts have been made to set-up long term homogeneous polar low climatologies. However due to the course resolutions of these reanalysis datasets, it is hard to build a reliable climatology for the small scale polar lows. Condron et al. (2006) used the Laplacian of the pressure field to detect mesocyclones and investigate the frequency of occurrence in the ERA-40 reanalysis dataset. Kolstad (2006) uses the same reanalysis to set up a climatology of favourable conditions for the formation of polar lows without explicitly detecting the mesoscale cyclones themselves. The favourable condition is taken to be cold air outbreaks with reverse shear conditions. As mentioned in section 2.1 these reverse-shear conditions were found to be favourable for polar low formation. Zahn and von Storch (2008) compiled a long-term polar low climatology from a dynamical downscaling of the 6 hour NCEP/NCAR re-analyses from 1948-2006, see figure 1b. Bracegirdle and Gray (2008) derived an objective polar low climatology of polar lows in the North Atlantic over a period of approximately 5 years.

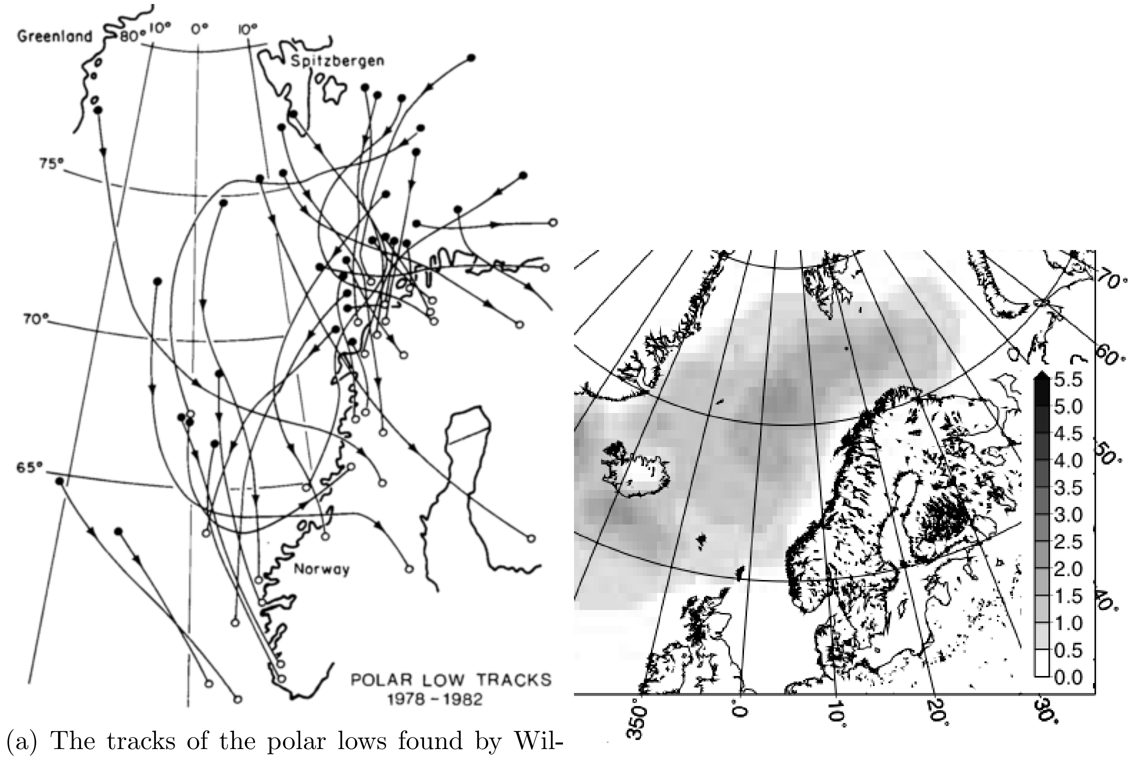

(a) The tracks of the polar lows found by Wilhelmsen (1985) by making use of satellite imagery, weather charts and synoptic observations.

(b) Polar low density per 250 km^2 from 1948-2006 as found by Zahn and von Storch (2008)

Figure 1

3 Dataset

We make use of the NORA10 dataset which is a high-resolution hindcast based on the Hirlam model running from 1970 to 2012. The domain is shown in figure 2, it includes the northeast Atlantic Ocean, the North Sea, the Norwegian Sea, the Barents Sea and parts of the Greenland Sea and Denmark Strait. The data is provided by the Norwegian Meteorological Institute. The following two subsections give a brief description of the model setup. For a complete description of the dataset, the reader is referred to Reistad et al. (2011).

3.1 Model setup

The model used is Hirlam, version 6.4.2 (see Unden et al. (2002)). The domain is set-up as a rotated spherical grid with the south pole at 22°S, 40°W with a resolution of 0.1° resulting in a horizontal grid spacing varying from approximately 10 to 11 kilometers. The number of gridpoints is 248 x 400. The model has 40 vertical hybrid levels, the vertical coordinate used gradually transforms from pressure coordinates at the top of the domain to terrain-following at the bottom. The model output which is available for our analysis is limited to seven vertical pressure levels at 100, 300, 500, 700, 850, 925 and 1000 hPa and the surface level. The model uses a prognostic equation for the turbulent kinetic energy (TKE) which includes both local and advective terms. Convective parameterization is achieved through a closure based on moisture flux convergence.

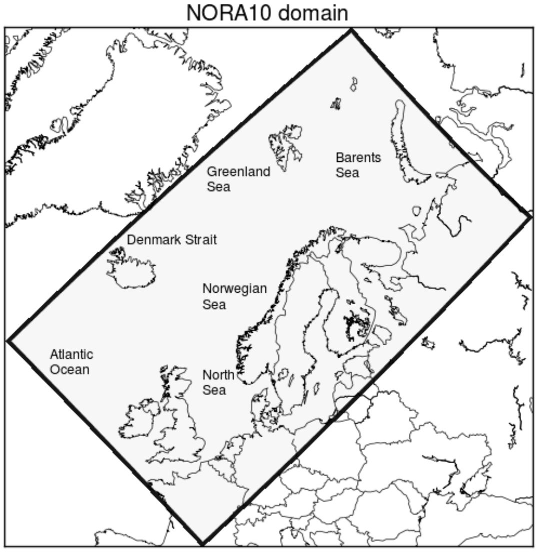

Figure 2: The NORA10 domain.

3.2 Boundary forcing and initialization

The model is forced at the boundaries by the reanalysis dataset ERA-40 (Uppala et al., 2005) for the period 1970-2002 and with the operational ECMWF analysis for the period 2002-2012. The meteorological fields imposed are temperature, specific humidity, wind and cloudwater at all vertical levels and surface pressure each 6 hours. Sea surface temperature, sea ice fraction and snow depth are also retrieved from ERA-40 or the operational ECMWF analysis.

A long sequence of 9 hour forecast runs is created every 6 hours where the initial fields within the domain of each cycle are a blend of ERA-40 and the 6 hour forecast of the previous NORA10 run. This procedure is used in order to preserve the small-scale features.

The initial fields from ERA-40 and the 6-hour forecast from the previous run (background field) have to be filtered before time integration can start. This filtering is needed in order to remove noise due to wind fields which are not in balance with the mass fields. These imbalances can grow and lead to numerical instabilities during the runtime (Huang and Yang, 2002). The difference between the filtered ERA-40 and filtered background field is then added to the background field to form the initial model state. The chosen type of digital filtering (Dolph) is known to perform best in preserving the initially fastest growing modes. The reader is referred to Huang and Yang (2002) for an overview of the performance of different digital filtering initialization options in HIRLAM.

4 Case study

In this section the NORA10 model performance on simulating a polar low is investigated by comparing model data against dropsonde observations within and in the environment of a polar low.

In February and March 2008 a three-week field campaign was conducted targeting polar lows and arctic fronts (Kristjánsson et al., 2011). Two polar lows have been studied by means of dropsonde observations, we will use a polar low developing a few hundred kilometres out of the Norwegian coast on the 3rd of March and hitting the Norwegian coast on the 4th of March 2008.

In section 4.1 the synoptic setting on these days will be described followed by a comparison of model data with observations in section 4.2.

4.1 Synoptic setting 3-4 March 2008

On the 2nd of March 2008 the combination of a high-pressure cell over Greenland and a low over the North Sea led to a cold-air outbreak over the Norwegian Sea. Within this cold-air outbreak, a convergence zone developed on the 3rd of March at the meridian stretching from the ice-edge at around 80 °N up to about 74 °N as can be seen in figure 3b. This convergence zone intersected another frontal zone which can be associated with the remnants of a dissipating depression. To the west of the north-south orientated convergence zone, cloud streets can be seen developing down-stream of the ice-edge and indicating the strong sea-air temperature contrast. Around the intersection of the two above-mentioned frontal zones, the polar low developed during the 3rd of March and reached its mature stage on the 4th of March while moving south-southeast towards the Norwegian coast.

4.2 Comparing model and observations

During the 3rd and 4th of March a total number of 55 dropsondes have been launched capturing the environment before the polar low developed on the 3rd of March, and the polar low itself on the 4th of March. This makes this case very well documented and a good case to assess the performance of NORA10. In order to make a good comparison between the observations and the NORA10 model, we first assess model performance in terms of simulating the polar low at the right location and time. In figure 3 we put the NORA10 fields side-by-side with infrared satellite images taken from Kristjánsson et al. (2011). The cloud fields are represented remarkably well in NORA10. Carefully comparing the times however, shows that the polar low in the model is ahead of time. At 12 UTC on the 4th of March, the polar low in the model is located just outside the Norwegian coast, which is approximately 200 km too far to the south-east. Since we are mainly interested in the structure of the polar low itself we try to compare the dropsonde observations to suitable model cross-sections through the polar low. Since the location of the polar low in the model on the 4th of March at 6 UTC is close to the dropsondes released on this day from 11 to 12 UTC, it is decided to take a crossection exactly through the core of the polar low in the model at this timestep.

Baroclinic zone Figure 4 shows the results for cross-section A, through the baroclinic zone on the 3rd of March from which the polar low would develop the next day. The observations show a low-level baroclinic zone with potential temperatures at the surface rising from 262 K to 274 K from west to east over a distance of about 200 km. NORA10 has similar horizontal gradients of potential temperature. NORA10 shows a very stable temperature profile between 500 and 400 hPa which can not be found in the observations. The colder air in the west in combination with the northerly background flow creates a southerly thermal wind and thus reverse shear conditions. This explains the strong northerly low-level jet of about 25 m/s at around 950 hPa in the observations. The model also shows this low-level jet, although its strength is underestimated with wind speeds of about 20 m/s. In terms of moisture the difference between model and observations is rather large. The model shows very dry conditions above 800 hPa in the eastern half of the cross-section, this can not be found in the observations. The results for cross-section B are presented in the

Appendix (figure 21), since the results are rather similar to cross-section A, which can be expected from the fact that both cross-sections intersect the same baroclinic zone.

The polar low In figure 5 the cross-sections through the polar low on the 4th of March are presented. The observations show a warm core located at around 400 km on the x-axis and extending from the surface up to about 450 hPa. NORA10 also shows this warm core, but it extends only from the surface up to approximately 800 hPa. Furthermore NORA10 overestimates the temperatures near the surface with about 4 K compared to the observations. Interestingly, one of the dropsondes was dropped in the cloud-free region in the center of the polar low. This shows very dry air from about 800 hPa and above, the high values of relative humidity surrounding 'the eye' and reaching to about 500 hPa can be associated with the convective towers. The model also shows this dry layer around the eye, but it slightly underestimates the convective activity surrounding the eye of the polar low.

The model has a significant error in timing of the polar low, however in terms of thermal structure and wind fields the polar low is well represented. Both the warm core structure as well as the winds are very good in agreement with the observations. The humidity fields show significant differences with the dropsonde observations, however when looking at the cloud fields from above in figure 3 it can be seen that the convective towers around the center of the polar low in the model are in accordance with the satellite observations. Due to the small spatial scales of the convective towers rotating around the polar low, it is not surprising that the model cross-section shows a different moisture profile than the dropsonde observations.

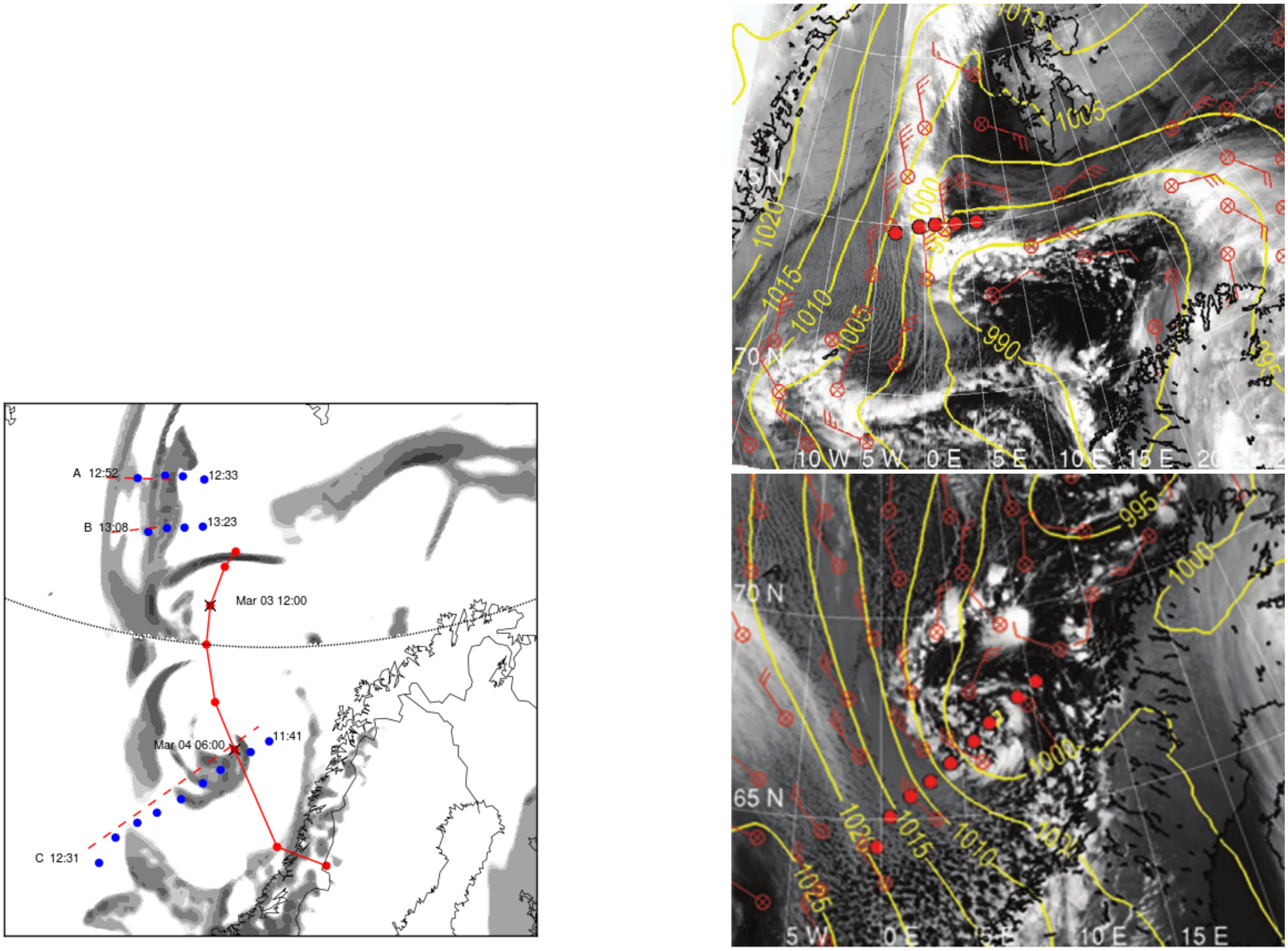

(a) (b)

Figure 3: (a) The track of the polar low according to NORA10 (connected red dots), labelled NORA10 cross-sections (red dashed lines) and the corresponding dropsonde observations (blue dots). The black crosses through the red dots indicate the polar low position at the two timesteps which have been used for comparing the model against dropsonde observations. An indication of the model cloud field (relative humidity values at 850 hPa exceeding 90%) is shown in grey shading, for two different timesteps (top: 3rd of March 12 UTC; bottom: 4th of March 6 UTC) seperated by the dotted line in the middle of the figure. Model crossections A and B - through the pre-polar low baroclinic zone - are taken at the 3rd of March 12:00 UTC and compared against dropsonde observations for the same day dropped between 12:33 UTC and 13:23 UTC. Model cross-section C - through the polar low - compares the model at the 4th of March 06:00 UTC against dropsonde obversations made on the same day between 11:41 and 12:31 UTC. (b) NOAA infrared satellite images of the low-level baroclinic zone on the 3rd of March at 12.00 UTC (top) and of the polar low on the 4th of March at 11.28 UTC (bottom). Sea-level pressure contours in yellow are from the Norwegian HIRLAM 12 UTC analysis and the red windbarbs show QuickSCAT winds. Red dots indicate dropsonde release positions (corresponding to cross-section B and C in figure a. Figures are taken from Kristjánsson et al. (2011).

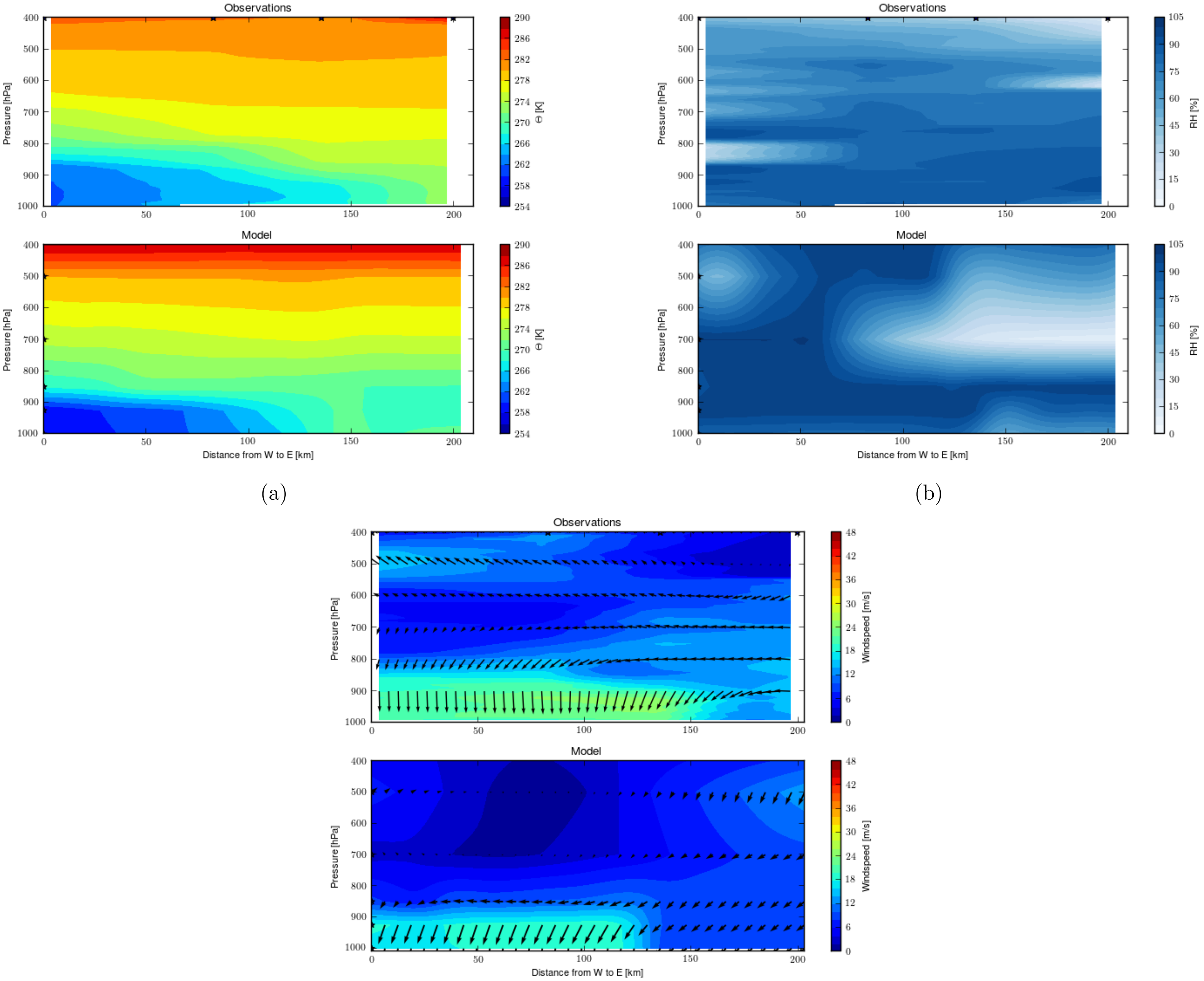

(a)

(b)

(c)

Figure 4: Crossections interpolated from dropsonde observations (top of each subfigure) and from the NORA10 model output (bottom of each subfigure) for cross-section 'A' (see figure 3a) through the low-level baroclinic zone on the 3rd of March at 12 UTC. The black stars indicate dropsonde locations and model pressure levels.

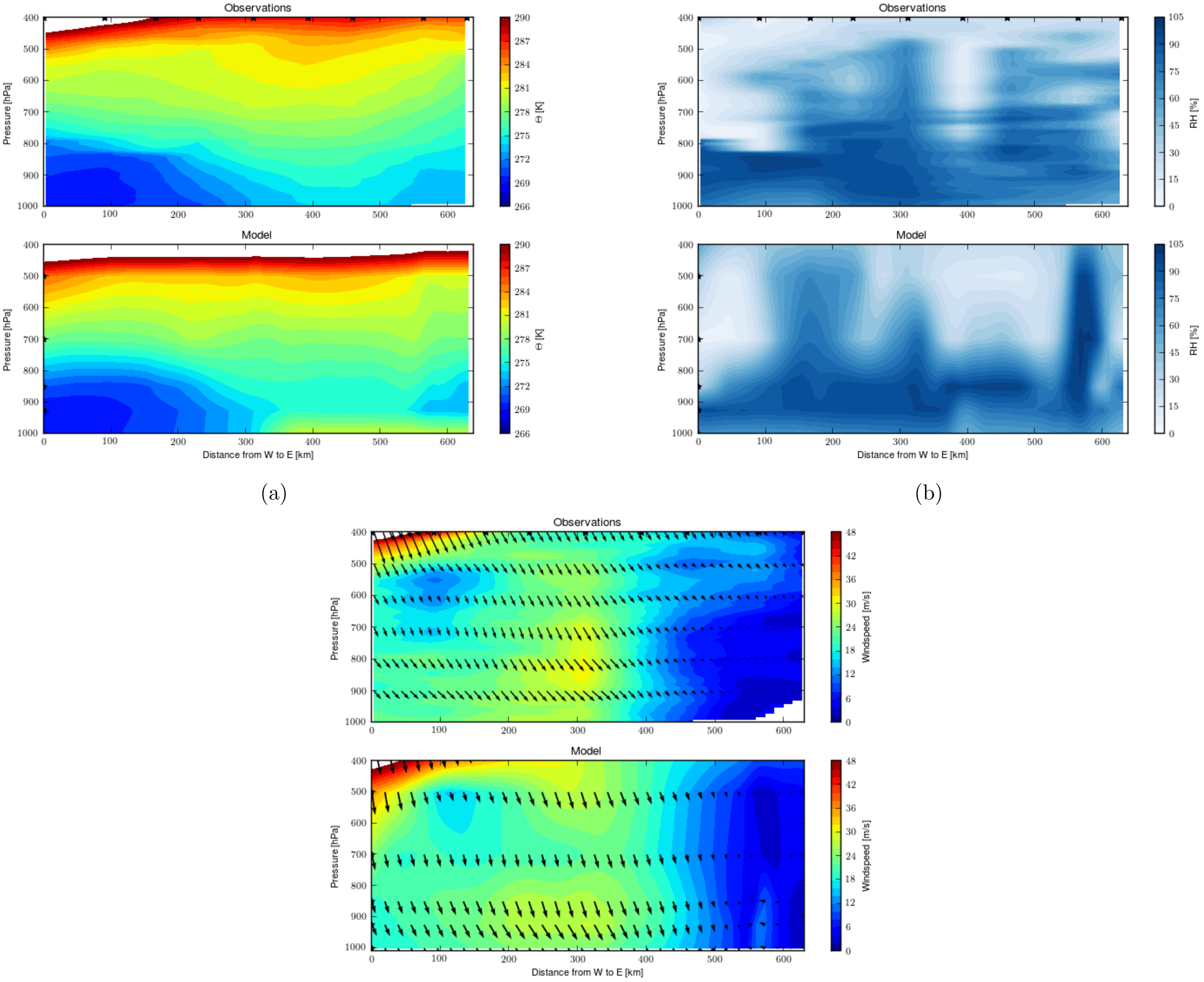

(a) (b)

(c)

Figure 5: Crossections interpolated from dropsonde observations (upper panels) and from the NORA10 model output (lower panels) for cross-section 'C' (see figure 3a) through the polar low on the 4th of March at 6 UTC. The black stars indicate dropsonde locations and model pressure levels.

5 Methods

This section can be split into three distinct parts. Section 5.1 describes the cyclone tracking scheme, section 5.2 describes the objective polar low identification and track selection and in section 5.3 the different parameters, which are used to study polar low structure and forcing, are presented. At the end of this section a case-study is presented where we apply the diagnostics to one of the polar low tracks.

5.1 The cyclone tracking scheme

Early approaches to cyclone tracking were manual. By drawing contour lines from observed sea level pressures, minima could be found by looking for closed contours in the hand-drawn weather maps. By identifying cyclones in consecutive timesteps a track could be reconstructed, subjective to the meteorologists interpretation. With the advent of numerical weather prediction, global datasets of sea-level pressure became available spanning longer periods. Especially the development of reanalysis datasets and the increase in computational resources allowed for the development of objective cyclone tracking schemes. Whereas most conventional cyclone tracking schemes have been designed to track cyclones in global datasets, our tracking scheme has to perform on a regional dataset. When starting to develop this tracking scheme, the author did not realise at all what a challenge it would be.

In general the cyclone tracking schemes can be broken down in different parts. First we are concerned with *detection* of the cyclones and - optionally - any *pre-processing* on the relevant meteorological fields. Once the cyclones are detected, the cyclone *tracking* is concerned with connecting the cyclones in different timesteps to construct the most likely tracks. Finally most cyclone tracking schemes include a *post-processing* part in which tracks are selected on certain criteria, for example the cyclone has to exist for a certain number of hours.

In the following subsections each of the above steps in the cyclone tracking algorithm will be discussed with reference to other tracking schemes and a motivation will be given for the choices made for the newly developed cyclone tracking scheme. For a review article and an intercomparison study on cyclone tracking schemes the reader is referred to Ulbrich et al. (2009) and Neu et al. (2012), respectively. The Python code of the cyclone tracker can be found in the Appendix.

5.1.1 Pre-processing and detection

Different approaches exist in detecting cyclones. Cyclones are either defined as minima in mean-sea level pressure (e.g. (Wernli and Schwierz, 2006)) or 1000 hPa geopotential height or as maxima in low-level vorticity fields (e.g. Hodges (1994)) or the closely related laplacian of pressure.

Hodges (1994) uses relative vorticity at the 850 hPa level for tracking features. The advantage of using this level relative to a surface level is that the vorticity field is not distorted by low-level features due to interaction with the surface (e.g. sea-breeze circulations, orographic jets).

A drawback of using relative vorticity (or the laplacian of pressure) for cyclone detection is that it is strongly dependent on the spatial resolution of the data. Murray and Simmonds (1991) find that some of the cyclones manually identified in synoptic weather charts at mid-latitudes in the southern hemisphere are not linked to a local minimum in sea-level pressure in the global circulation model. However at these locations they do find a local maximum in the laplacian of mean sea-level pressure. In this occasion, for a maximum in pressure laplacian without a minimum in mean sea-level pressure, they connect this point with a minimum in pressure gradient which can be argued to be the most likely position of a cyclone which is unresolved by the model. It has to be noted that this early global circulation model had a course resolution of approximately 500 km. For our dataset with a resolution of 10-11 km we can be sure that the polar lows with typical sizes of 500-700 km (diameter) will be resolved, thus there is no need for interpolation.

Since polar lows are phenomena with the main occurrence in the lower atmosphere, it is decided that the tracking algorithm will be based on a surface field. The relative vorticity of the 10m winds could be a candidate, however as mentioned above, the interaction of the wind with the surface causes maxima in vorticity, which are not necessarily linked to a cyclone. Further it was found that in our dataset, with 10-11 km horizontal resolution, the vorticity values near frontal zones were of similar magnitude as the cyclone centers, providing another challenge. Mainly for this reason, it was decided not to use relative vorticity. The remaining candidates are the 1000 hPa geopotential height or mean sea-level pressure which are equivalent to each other under hydrostatic equilibrium. It is decided to use the mean sea-level pressure field.

The cyclones are associated with local minima in mean-sea level pressure. For determining the local minima, the value of mean sea-level pressure has to be compared to neighbouring gridpoints, which is called the neighbourhood. A neighbourhood consisting of 4 gridpoints is referred to as a Moore neighbourhood, while the 8 gridpoints neighbourhood is the 'Von Neumann' neighbourhood. It was found that the most strict 'Von Neumann' neighbourhood produces about half the amount of minima when compared to the less strict Moore neighbourhood. See figure 6 for the minima found in one single timestep for the different neighbourhoods.

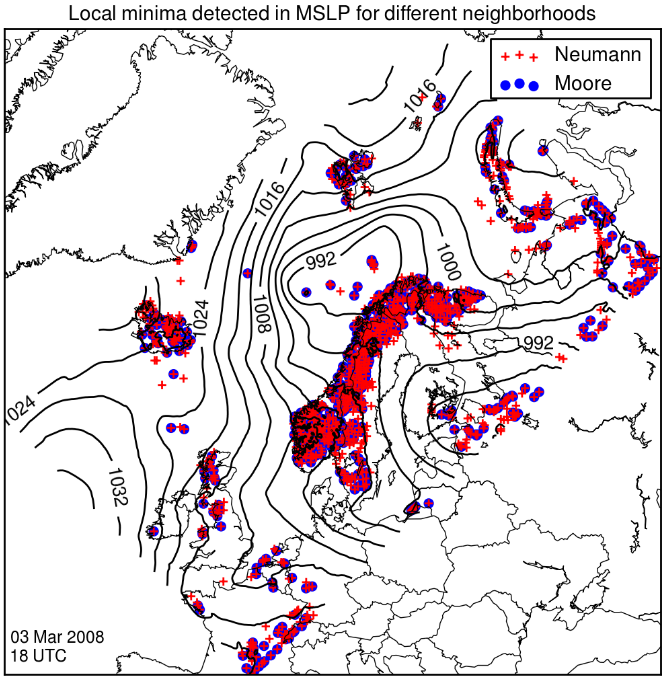

Figure 6: The detected minima in mean sea-level pressure (MSLP) for different neighbourhoods on the 3rd of March 2008 at 18 UTC. The Neumann neighbourhood consists of the 4 neighbouring gridpoints, while the Moore neighbourhood consists of 8 neighbouring gridpoints.

From now on we use the most strict condition of 8 neighbouring gridpoints like Wernli and Schwierz (2006) do. A well-known problem is the high number of local minima that are found. Due to errors in reduction to mean sea-level pressure, spurious minima pop up over higher elevation terrain. For this reason, some authors do not take into account the minima found over high elevation terrain. Pinto and Spangehl (2005) erase all minima above an elevation of 1500m. However for our high-resolution dataset (with high-resolution representation of topography) minima occur over lower elevations as well. Since we are interested in polar lows - which are known to be maritime cold air cyclones - a more rigorous approach could be to erase all minima occuring over land.

However, we have to realise that the high-resolution of NORA10 has the consequence that also spurious minima are detected over islands. For these regions it would be hard to distinguish from a real polar low or an artificial low which can be related to mean sea-level pressure reduction errors above topography. It is clear that erasing all detected minima occurring over land is not a good approach.

Alternatively a threshold can be put on the value of the local minima compared to the value of a certain number of points surrounding the minimum. This approach was tested, but it was found not to have the desired outcome of distinguishing between the real cyclones and the artificial lows related to the sea-level reduction errors.

Another potential method for distinguishing the artificial lows from the real cyclones is the watershed segmentation. Muskulus and Jacob (2005) uses a watershed segmentation algorithm on the mean sea-level pressure field as a measure for the area under influence of a certain cyclone. In a watershed segmentation, all the gridpoints are removed from their original position in the two-dimensional field. After this they are sorted on their values. Starting with an empty grid, the gridpoints are put back one after the other, starting with the lowest values. When a gridpoint is put back at a position where it is not adjacent to another point, a new region is started. If a point is adjacent to another gridpoint, this point is added to this region. When a gridpoint is put back and is adjacent to two or more points from distinct region, the point is marked as a watershed border. The watershed segmentation algorithm thus simulates a flooding of the mean sea-level pressure 'landscape'.

Since the artificial lows over topography are a footprint of the local topography, their watershed area would probably be very small. If this would be the case, a threshold could be put on the watershed area for each minima, thereby making it possible to distinguish between real cyclones and artificial lows. For this reason the watershed segmentation was performed for a few time steps.

Unfortunately the watershed segmentation seems not to be the preferred method for distinguishing between artificial lows and real cyclones. As can be seen by visual inspection of the watershed areas (see figure 7), the problem is that the watershed region of artificial lows over islands extents far outside the islands. Apparently a low gradient region connects to these lows. Since the watershed area of these artificial lows is comparable to that of real cyclones, no suitable threshold can be found to filter them out. Thus it is decided not to use the watershed segmentation for cyclone detection and selection.

Since the artificial lows are a footprint of the topography, they are very small scale features with typical length scales in the order of the model grid spacing. A straightforward way of getting rid of these lows would be a low pass filter on the mean sea-level pressure field. This low pass filter can be incorporated by smoothing the field with a suitable filter and smoothing radius. This method was initially not preferred, because the smoothing effectively reduces the resolution of the data.

However, since all of the above approaches were proven not to be of use for our purpose and this dataset, it was decided to smoothen the pressure field with a Gaussian filter. The smoothing radius was chosen to be 5 gridpoints, or approximately 55 km. Since a typical size for a polar low is 200-1000 km in diameter (Rasmussen and Turner, 2003), the smoothing will not erase features that we are interested in.

The cyclone detection is based on all the local minima in the smoothed mean sea-level pressure field. In the next section it will be discussed how the cyclones in subsequent timesteps are connected to form the tracks.

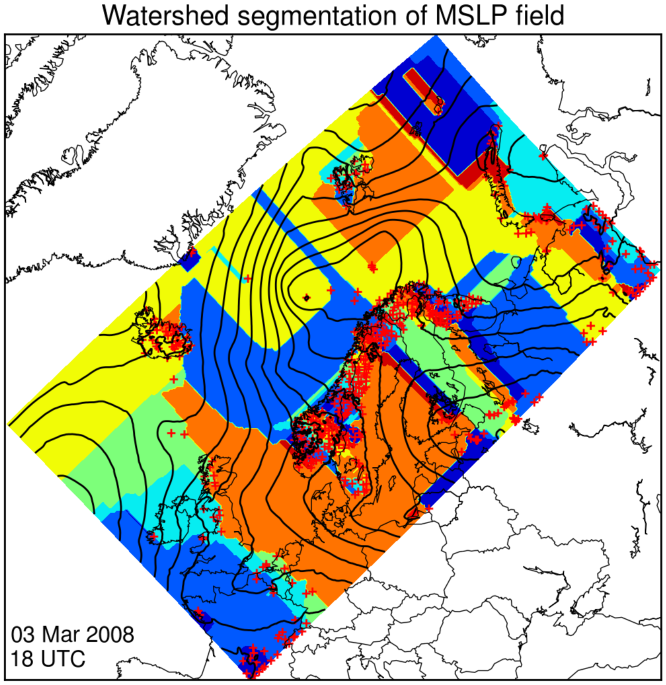

Figure 7: A watershed segmentation of the mean-sea level pressure (MSLP) field for the 3rd of March 2008 at 18 UTC. Different watershed regions are marked with a different color. Red crosses denote the minima found using the 8-point neighbourhood.

5.1.2 Tracking Algorithm

The tracking algorithm is concerned with connecting the cyclones in different time-steps to construct cyclone tracks. Our tracking scheme is based on maximizing the summed likelihood of all possible connections between lows in two consecutive timesteps. The scheme allows for both the development (cyclogenesis) as well as the disappearance (cyclolysis) of cyclones. The scheme does not allow for the merging or splitting of cyclones.

Considering two consecutive timesteps at time t_q and t_{q+1} we name all the cyclones in timestep t_q the *parents* and all the cyclones in timestep t_{q+1} the *childs*. A connection between a parent and child is called a segment and denoted with s. For N_p parents and N_c childs we can make $N_s = N_p \cdot N_c$ different segments:

$$S = \{s_1, s_2, s_3, ..., s_{N_s}\} \tag{1}$$

With S the collection of segments. We reduce this total number of segments by applying a distance threshold for each segment in S. The distance threshold is seperated into a maximum allowed meridional displacement σ_y and a maximum allowed zonal displacement σ_x. We still refer to set S and note that from now on we reduced the number of segments such that $N_s \leq N_p \cdot N_c$. The motivation for choosing a different threshold

for the zonal and meridional directions, is that there exists a strong difference in the maximum speed a cyclone can reach in the zonal direction compared to the meridional direction. For now, the performance of the cyclone tracking scheme was checked manually and a good performance was found for a distance threshold of 500 km in both the zonal and meridional direction.
We now calculate for each segment a likelihood L, which is a gaussian function of the distance between parent and child, the gaussian is shaped according to the distance thresholds (σx,σy) used.

$$L(\Delta x, \Delta y) = \frac{1}{2\pi\sigma_x\sigma_y} e^{-\frac{\Delta x^2}{2\sigma_x^2}-\frac{\Delta y^2}{2\sigma_y^2}} \tag{2}$$

The final track has to be constructed from the most likely combination of segments. A trackset τ is defined as a collection of n_s segments. To start with, we choose n_s to be $min(N_p, N_c)$. In which case either all parents are connected to one child, or all childs are connected to one parent. The total number of tracksets τ when choosing n_s segments out of the N_s segments is then given by the binomial coefficient.

$$\binom{N_s}{n_s} = \frac{N_s!}{n_s!(N_s - n_s)!} \tag{3}$$

For a typical value of $N_s = 14$ and $n_s = 5$ this already gives 2002 different tracksets τ. We select the combinations on the condition that the segments in each trackset have to be unique in both their parent and their child. In other words, we do not allow for the splitting or merging of cyclones. This reduces the number of tracksets to only a few. The selected tracksets τ are collected in a tracksetcollection T:

$$T = \{\tau_1, \tau_2, \tau_3, ..., \tau_{N_\tau}\} \tag{4}$$

The trackset has to be interpreted as all the possible ways to connect the parents and childs under the distance threshold. For each trackset τ we can calculate the likelihood by summing the likelihood of each segment in τ. Since we allow for the development and disappearance of cyclones the number of segments in the trackset does not necessarily have to be equal to $max(N_p, N_c)$, it could be smaller as well.

$$n_s \leq max(N_p, N_c) \tag{5}$$

Since lowering the amount of segments changes the possible combinations, it is possible given a set of N_s segments that a trackset τ with a lower number of segments n_s has a higher likelihood than a trackset with a higher number of segments.
The collection of tracksets T is thus expanded by adding all other tracksets for all values of n_s that satisfy the criterion mentioned above. Finally the trackset in T with the highest likelihood is taken as 'the right' one and used to connect the parents and childs in the most likely way.
It was found that the above described algorithm is computationally very expensive. This is related to the number of possible tracksets which rises very fast with an increasing number of allowed segments (see equation 3). This results in almost one million different combinations.
Although thresholds are used on the allowed distance between parents and childs, this is not fully exploited, since maximizing the likelihood is done over the complete set of segments. When we plot one set of parents and childs and the allowed segments, we recognize different groups of parents and childs. Where a group is defined as a set of parents and childs where each member of the set can be reached by traversing the allowed segments. If we maximize the likelihood per group of parents and childs, we significantly reduce the number of combinations and thereby increase the computational efficiency of the cyclone tracking algorithm.
The grouping of parents and childs in connected regions is achieved by performing a depth-first search in a recursive algorithm. The algorithm starts by picking a parent or child and from this parent or child it

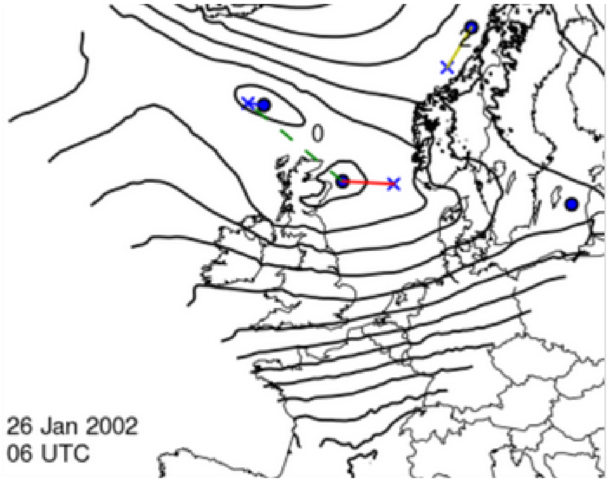

Figure 8: An illustration of the working of the cyclone tracking algorithm. The black contours show the pressure contours on the 26th of January 2002 at 6 UTC. The blue dots represent the cyclones corresponding to this timestep (parents), while the crosses represent the cyclones in the next timestep (childs). First the cyclones are split into different groups based on a distance threshold. In this example two different groups can be found, labelled with 0 and 2. Also there is one isolated parent, which is related to cyclolysis or a movement of the cyclone out of the domain. For each group, all allowed segments are drawn (dashed lines) and the most likely combination of segments is choosen (solid lines).

finds the next one via an allowed segment. It 'travels' to all connected parents and child along the allowed segments until there is no segment left (depth-first). Then it jumps back (using recursion) to the last point where there were more unexplored segments and descends this branch to the end. All the parents and child found in one depth-first search are labelled with the same number. After this, a next parent or child is picked and if it is not labelled to be in a group yet, a depth-first search will be started from this parent or child and a new group is created. The depth-first search is an efficient algorithm and the computing time scales linearly with the number of allowed segments. Typically three or four different groups were found, reducing the number of tracksets by one to three orders of magnitude.

The working of the cyclone tracking algorithm is illustrated in figure 8. By connecting the found segments for each combination of two consecutive timesteps over time, the final tracks are constructed.

5.2 Objective polar low identification

This section describes the method used to objectively identify polar lows in our dataset and how this is applied to the tracks to identify polar low tracks and define different life-stages along the track.

A few authors have studied polar lows in high-resolution datasets. Xia et al. (2012) compared two different identification and tracking methods which both use a spatial filter on the mean sea-level pressure or vorticity fields. The tuning of the filters to our dataset would be a huge effort, and for the sake of time it was decided not to use these methods for polar low identification. Bracegirdle and Gray (2008) use another polar low identification method which detects strong cyclones occurring in a marine cold-air outbreak. They showed that the difference between the 700 hPa wet-bulb potential temperature and the sea surface temperature is an effective discriminator between conditions associated with polar mesocyclones and other cyclones in the Nordic seas. An additional threshold on the vertical component of the relative vorticity of the 10m winds, assures that the cyclone is strong enough to be classified as a polar low. Comparing the objective climatology to a database of subjectively identified polar lows in the Nordic seas showed satisfying results in terms of total counts as well as the spatial distribution.

ζ_0	NORA10	BG
0.00	2630	5709
0.65 x 10^{-4} s^{-4}	1870	1892
1.35 x 10^{-4} s^{-4}	835	390

Table 1: Sensitivity of marine cold-air cyclone counts to relative vorticity thresholds for our study [NORA10] compared to Bracegirdle and Gray (2008) [BG].

We follow the method by Bracegirdle and Gray (2008) (hereafter BG) in identifying polar lows thus the constraints for a cyclone to be identified as a polar low are as follows:

1. The cyclone must occur over sea.
2. The cyclone must occur in a cold air outbreak: $\theta_{w700} - SST \leq -2.8K$
3. The cyclone must exceed a threshold intensity in terms of relative vorticity: $\zeta > \zeta_0$

The vorticity threshold chosen by BG was based on the observation of Wilhelmsen (1985) that - for a 50 km horizontal gridspacing - this value corresponds to polar low motion-relative surface wind speeds of about 5 m/s. Since values of relative vorticity are highly sensitive to horizontal resolution, it was decided to interpolate the surface winds of NORA10 to this 50 km horizontal gridspacing in order to allow for using the same vorticity threshold as BG.
First we compare our results against BG by testing the sensitivity of cyclone counts on the vorticity threshold used, over the same period as BG. We apply the first two criteria mentioned above, such that we are looking at marine cold-air vortices, and test sensitivity to the vorticity threshold. Note that multiple counting will occur, since the same polar low will be counted in different timesteps. The domain of BG is somewhat different from our domain, it includes the Denmark Strait and the Labrador Sea. Also the timestep is 12 hours for BG and 6 hours for our data. This makes it impossible to compare the number of cyclone counts. We can though compare the sensitivity to the vorticity threshold used, between BG and our dataset. Table 1 shows the total number of marine cold-air vortices for NORA10 and BG over the same period from the 1st of January 2000 to the 30th of April 2004. For the same vorticity threshold of 1.35 x 10^{-4} s^{-1} we find a number of 835 cyclones, whereas BG finds only 390. The difference of about a factor 2 can be explained by the fact that the dataset of BG has a timestep of 12 hours whereas our dataset has a 6 hour time resolution.
Lowering the threshold increases the number of cyclones, but not as much as in BG. A possible explanation for this could be the smoothing before the minima detection as described in section 5.1.1, which means that the weakest cyclones existing in our dataset are not detected. Since the number of counts for a threshold of 1.35 x 10^{-4} s^{-1} corresponds well to BG and also the geographical pattern is similar (not shown), it is decided to use the same threshold.

Polar low track selection and life-stages The cyclone tracking schemes tracks all cyclones, regardless whether or not they satisfy the polar low criterium. When the cyclone satisfies for at least two consecutive timesteps the polar low criterium along its track, this track is selected as a polar low track.
Now we can define different life-stages of the polar low along its track. First, we define the 'mature' stage, which is the point along the track where the polar low reaches the highest intensity as measured in terms of relative vorticity. From this point we can travel back in time along the track to find the 'begin' stage of the polar low. For detecting this begin stage, we use the same criteria as for the polar low, but we lower the vorticity threshold to half the value used for the polar low criterium. This implies that we detect strong meso-scale cold-air vortices which later grow into a polar low. Choosing this vorticity threshold is somewhat arbitrary, and it would be interesting to investigate how track length and duration depend on

the choosen vorticity threshold for the begin stage. In addition to the 'begin' and 'mature' stage we can define an 'end' stage as the first point after the mature stage which does not satisfy the polar low criterium anymore, or the last point of the track if all the points satisfy the polar low criterium.
Summarizing, we define the following three life-stages for each polar low track:

1. Begin: The first point along the track before the 'Mature' stage which satisfies the criterium for a mesoscale cold-air vortex
2. Mature: The point with the highest value of relative vorticity which satisfies the polar low criterium
3. End: The first point after the 'Mature' stage which does not satisfy the polar low criterium anymore or the last point of the track if all points satisfy the polar low criterium

5.3 Diagnostics

In this section we present the diagnostics applied to the polar low tracks that we obtained. In section 5.3.1 the parameters related to the *thermal structure* of the polar lows are presented, followed by the parameters related to *forcing* of the polar lows in section 5.3.2.

5.3.1 Structure parameters

The investigation of cyclone structure will be done using two parameters which have originally been developed for the analysis of tropical and extra-tropical cyclones and the transition between these two types (Hart, 2003).

Thermal asymmetry The thermal asymmetry parameter is defined as the storm-motion relative thickness gradient across the cyclone. The relative thickness is the distance between two pressure surfaces and is thus a measure for the average virtual temperature[1] in this column of air. The gradient is taken across the cyclone by taking the difference in thickness values between the right and left semi-circle for a chosen radius with respect to the storm motion. The equation for this thermal asymmetry TA is as follows:

$$TA = (\Delta Z_{right} - \Delta Z_{left}) \tag{6}$$

With ΔZ the relative thickness, which is the difference in geopotential height between two pressure surfaces. See table 2 for the different levels. The thermal asymmetry parameter allows to distinguish between normal-shear and reverse-shear situations as described in section 2.2. Negative values of TA imply that the warm air is to the left of the cyclone. In the northern hemisphere the thermal wind has the warm air at its right hand side. Thus the thermal wind opposes the storm motion, which implies that negative values of TA correspond to reverse-shear conditions.

Thermal core The thermal core parameter is designed to give insight in the thermal structure of the core of the cyclone. The thermal structure of the core and the change of cyclone strength with height are directly related to each other through the thermal wind relation. This parameter is calculated by taking the derivative of the geopotential height gradient at an isobaric surface with respect to height.
First the gradient in geopotential height for a certain isobaric surface is calculated. This gradient (Φ') is calculated by taking the maximum geopotential height (Φ_{max}) minus the minimum geopotential height (Φ_{min}) within a certain radius 'd'. This gradient is proportional to the magnitude of the geostrophic wind.

$$\Phi' = \Phi_{max} - \Phi_{min} \tag{7}$$

---

[1] The virtual temperature accounts for the density increment due to moisture in the air.

$$\Phi' = \frac{dg \mid V_g \mid}{f} \tag{8}$$

With f the Coriolis parameter, g the gravitational acceleration and d the distance between the maximum and minimum in geopotential height. Now we can define the thermal core parameter TC as the vertical derivative of this quantity in (logarithmic) pressure coordinates.

$$TC = \frac{\Delta\Phi'}{\Delta ln(p)} \tag{9}$$

Where Φ is the geopotential height and p is the pressure. Note that the derivative is taken with respect to (the logarithm of) pressure which decreases with height. This means that the TC parameter is proportional to the negative of the thermal wind with the scaling factor determined by equation 8. Positive values of TC correspond to a warm core, while negative values of TC correspond to a cold core.

Choosing a suitable radius Both structure parameters are calculated over a certain radius surrounding the cyclone center. The two structure parameters - thermal asymmetry and thermal core - are designed to capture ambient baroclinicity relative to the storms motion and the thermal structure of the core respectively. A suitable radius would be such that it contains the largest part of the convergent inflow of the polar low, but not too large to prevent inclusion of other nearby cyclones. Hart (2003) uses a radius of 500 km for diagnosing (extra-)tropical cyclones. Scaling this ratio proportional to the size-ratio for (extra-)tropical cyclones versus polar lows, we find a radius of 120 km. Ideally, with the large range in polar low sizes, the radius used would depend on the polar low size. However, since no straightforward method exists for objectively determining the polar low size, it was decided to chose a constant radius.

Choosing suitable model levels Hart (2003) uses the levels 900-600 hPa and 600-300 hPa for calculating the phase-space parameters. Since polar lows are rather shallow systems with the strongest signature in the lower troposphere (Rasmussen and Turner, 2003), we decide to use lower levels. We define the 'low' level as the 1000-850 hPa level, the 'mid' level as the 850-500 hPa level and the 'upper' level as the 500-300 hPa level. Although we only detect cyclones occurring over sea, small extrapolation errors can be introduced for the 'low' level parameters when mean sea-level pressure values are below 1000 hPa. However with a full layer thickness of 150 hPa, the error introduced by this extrapolation is assumed to be small.

5.3.2 Forcing parameters

Baroclinicity Baroclinic instability is one of the proposed mechanisms for polar low genesis. The thermal asymmetry parameter as described in section 5.3.1 is closely related to baroclinicity. However this parameter calculates the gradient in geopotential thickness perpendicular to the storm motion vector. As described in section 5.3.1 this parameter can take both positive and negative value depending on the alignment of the geopotential thickness gradient with the storm motion. In case of a velocity vector perpendicular to the gradient, this will result in a zero-valued thermal asymmetry parameter, while the polar low environment is baroclinic. To get around this issue, we define an additional parameter measuring the difference between the maximum and minimum geopotential height over the radius chosen. So by definition this parameter only takes positive values and is an absolute measure for the baroclinicity in the polar low environment.

$$BARO = (\Delta Z_{max} - \Delta Z_{min}) \tag{10}$$

Surface fluxes Surface fluxes of sensible and latent heat can contribute to polar low development. We define the surface flux parameter as the average value of the surface fluxes in a radius R around the polar low.

Vertical instability Several parameters can be designed to assess the vertical instability of the air in the environment of the polar low. Since polar lows are accompanied with moist convection, we choose the potential instability as a parameter, thus including the effect of latent heat release on buoyancy. We define two different instability parameters, both reaching from a bottom level up to the 700 hPa level. First we define the 'air instability' as the difference between the wetbulb potential temperature at 700 hPa and the wetbulb potential temperature at 925 hPa. Second, we define the 'air-sea instability' as the difference between the sea surface temperature and the 700 hPa wetbulb potential temperature. Note that for the second parameter, we use the sea surface temperature, whether or not the air can attain a wetbulb potential temperature close to the sea surface temperature is determined by the strength of the air-sea interaction.

$$\text{Air instability: } \theta_{W700} - \theta_{W925} \tag{11}$$

$$\text{Air-sea instability: } \theta_{W700} - SST \tag{12}$$

Parameter	Description	Model	Level(s)	Radius
TA_L	Thermal Asymmetry	NORA10	1000-850 hPa	120km
TA_M	Thermal Asymmetry	NORA10	850-500 hPa	120km
TC_L	Thermal Core	NORA10	1000-850 hPa	120km
TC_M	Thermal Core	NORA10	850-500 hPa	120km
TC_U	Thermal Core	NORA10	500-300 hPa	120km
B_L	Baroclinicity	NORA10	1000-850 hPa	120km
B_M	Baroclinicity	NORA10	850-500 hPa	120km
SHF	Surface Heat Flux	NORA10	surface	120km
-	Air instability	NORA10	$\theta_{W700} - \theta_{W925}$	-
-	Air-sea instability	NORA10	θ_{W700}-SST	-

Table 2: Overview of the several parameters related to polar low structure and forcing and the model levels used.

5.4 Case: The 1979 Dutch polar low

Before analysing the full dataset, the methodology is applied to one polar low case. The case chosen is a polar low hitting the Dutch coast on the 2nd of January 1979. This polar low caused hazardous conditions in The Netherlands with strong snowfall in the middle part of the country and gale force winds in the western part causing widespread damage to boats. The lowest pressure measured in Hoek van Holland was 1007 hPa.

In figure 9a the track of the polar low is shown together with the low-level geopotential thickness fields surrounding the low. The velocity vector determines the orientation of the two semi-circles. As mentioned in section 5.3.1 the thermal asymmetry (TA) parameter is calculated by first calculating the average value of the geopotential thickness for each semi-circle and then subtracting the value of the left semi-circle from the right-semicircle. In this case, the polar low has the warm air to its right, and is thus aligned with the thermal wind, which means that this polar low occurs in a forward shear environment. Interesting enough the thermal asymmetry for this polar low increases during its life-cycle, from a value of 6 near Scotland to a value of 15 before it makes landfall at the Dutch coast. This seems to be related to the polar low moving into the cold air reservoir which is located over the European continent. In figure 9b the evolution of the thermal asymmetry parameter and thermal core parameter are plotted against each other, thereby showing the movement of the cyclone through the phase-space.

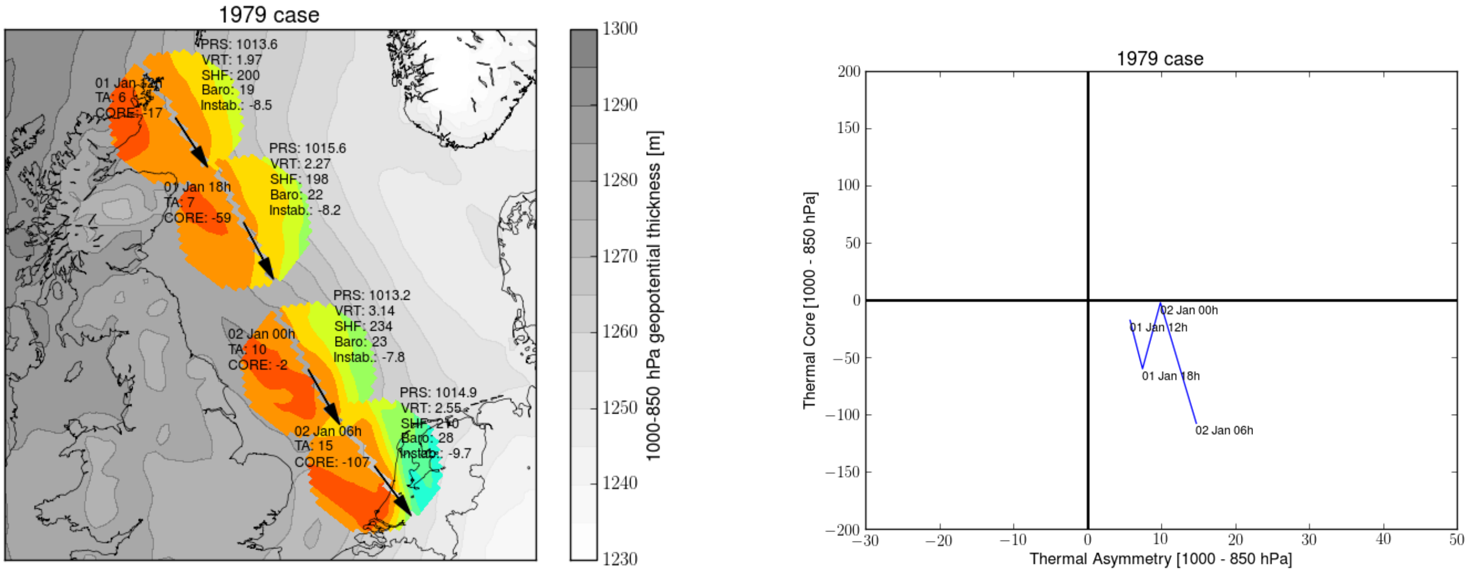

(a)

(b)

Figure 9: (a) Grey shading shows 1000-850 hPa geopotential thickness at the mature stage of the polar low (at 2 January 00h). The arrow shows the polar low motion vector surrounded by the two semi-circles which are used for calculating the thermal asymmetry parameter. The semi-circles are coloured with the geopotential thickness at the timesteps corresponding to the polar low position. To the left of the polar low the values of the structure parameter are shown in text: thermal asymmetry (TA) and thermal core (CORE). At the right side several other parameters are shown: central pressure (PRS), relative vorticity (VRT), surface heat flux (SHF), baroclinicity (Baro) and air-sea instability (Instab.). (b) The track of the polar low in the phase-space, with the timesteps shown.

6 Results

Over the period 1970-2012 we find a total number of 12097 polar low detections. These are all the detected MSLP minima which satisfy the criterium for a polar low. From these 12097 polar low detections, 2119 polar low tracks can be constructed. The difference between these numbers is explained by the fact that one polar low track contains several polar low detections and that some polar low detections are not contained in a polar low track.

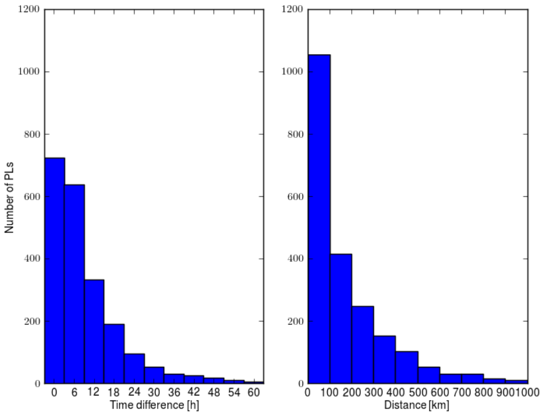

Figure 10: Histograms for the time (left) between the 'begin' and 'mature' stage and the distance travelled (right) between 'begin' and 'mature' stage for all polar low tracks.

For each of the polar low track a 'begin' stage and 'mature' stage are determined. In figure 10 histograms are shown for the time between these two stages and the distance travelled. Apparently, about 700 out of the 2119 have the maximum intensity at the first point of the track, which implies that the 'begin' stage is equal to the 'mature' stage. The majority of the polar lows take less than 24 hours to intensify, but the distribution has a long tail up to 60 hours. For distance travelled between the 'begin' stage to the 'mature' stage we find a similar pattern with most polar lows travelling less than 200 km, and a long tail up to about 1000 km. These statistics show that the set of polar low tracks is rather inhomogeneous in terms of track length. Studying the life-cycle of the polar lows would require a more detailed examination of this track length. More specific, the sensitivity of the track length to the vorticity thresholds for detecting the 'begin' stage and the distance thresholds in the tracking algorithm should be tested. For this reason, the main part of our analysis will be based on the 'mature' stage, which is very well defined as the stage where the polar low reaches its maximum intensity in terms of relative vorticity. We will briefly include the 'begin' stage to study changes of polar low structure and to identify polar low genesis regions. In section 6.1 the polar low climatology is presented in terms of total frequency and seasonal cycle. In sections 6.2 and 6.3 the results for polar low structure and forcing mechanisms are presented, respectively.

6.1 Climatology

By counting for each grid-point the number of polar lows within 200 km over the period 1970-2012 a long-term polar low climatology is constructed. This climatology is presented in figure 11. The polar low frequency corresponding to the 'begin' stage can be interpreted as the polar low genesis frequency. The 'mature' stage climatology shows the regions where the polar lows reach their maximum intensity in terms of surface relative vorticity. Maxima in polar low genesis are found to the southwest of Iceland, to the south-west of Svalbard and in the northeastern Norwegian Sea and Barents Sea. The maxima correspond to approximately 2.5 counts per year within a 200km radius. The climatology in terms of the 'mature' stage, shows overall the same pattern, although the polar low maximum in the Norwegian Sea is stretched much more to the south along the Norwegian coast.

In figure 12 we present the monthly climatologies for polar low cyclone center counts for the four most active months: December, January, February and March. The climatologies for the other months can be found in the appendix (figures 22 and 23).

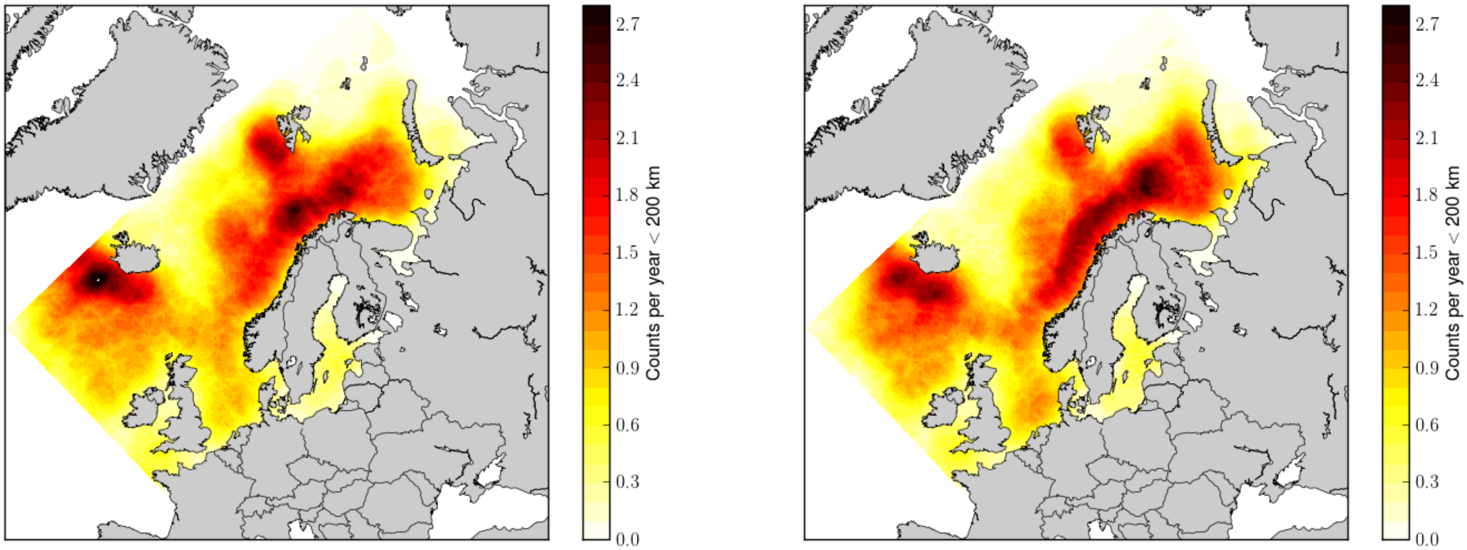

(a) Begin

(b) Mature

Figure 11: Polar low frequencies in counts per year within a radius of 200 km of each gridpoint for the 'begin' stage and the 'mature' stage of all 2119 polar lows.

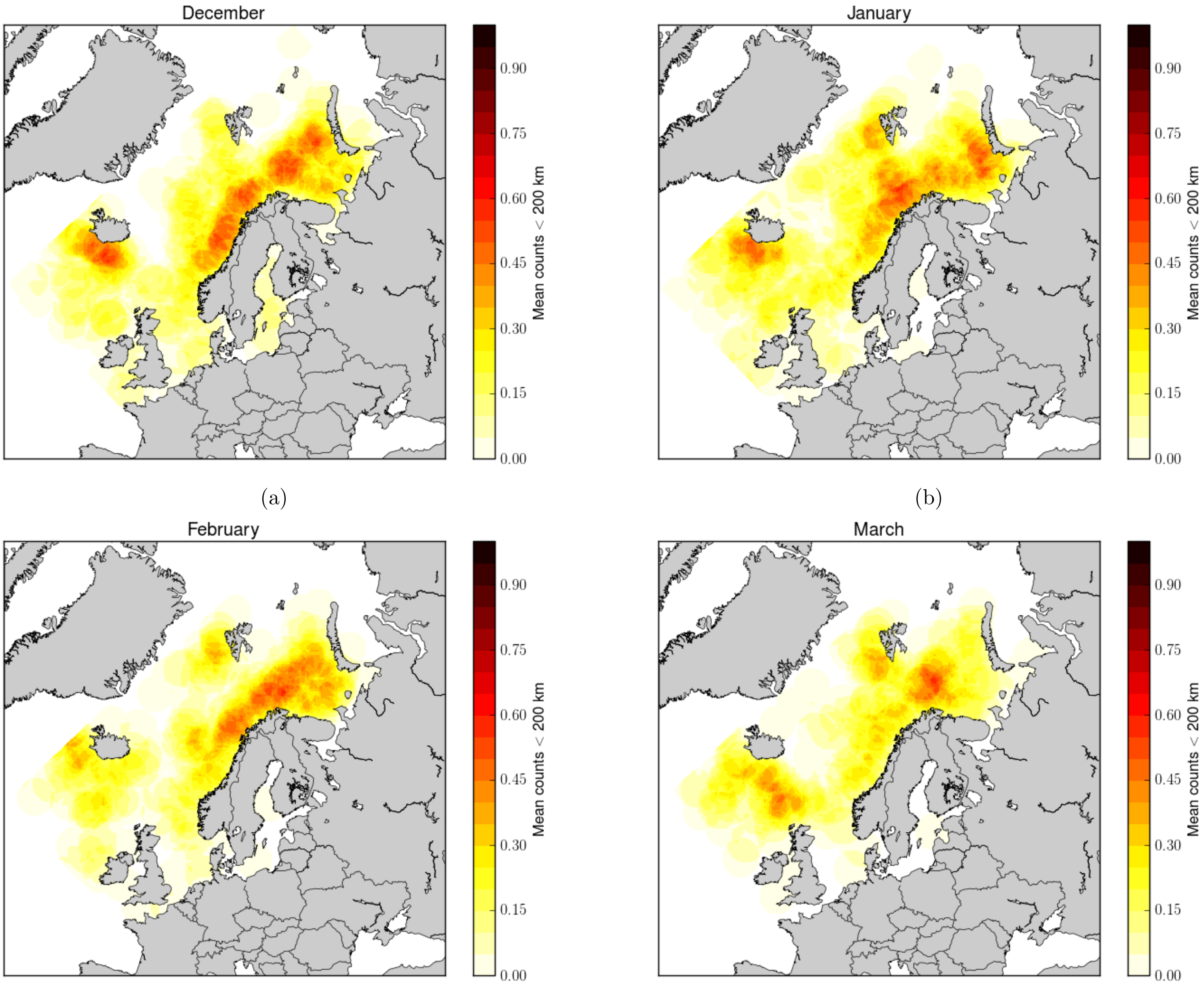

(a) (b) (c) (d)

Figure 12: Mean polar low detections within a radius of 200 km of each gridpoint per month from 1970-2012 for the months (a) December, (b) January, (c) February and (d) March.

6.2 Structure

Figure 13 shows box-and-whisker plots for the two parameters related to the structure of the polar lows in the 'begin' stage and the 'mature' stage. In terms of thermal asymmetry there is a remarkable small difference between the 'begin' stage and the 'mature' stage. The majority (75%) of the polar lows has a positive value of the thermal asymmetry corresponding to a forward shear environment at both the low and mid levels. For the core parameter we find that the polar lows in the 'mature' stage tend to have a warmer core at low levels than in the 'begin' stage. About 70% of the polar lows have a warm-core structure at low levels in the mature stage. At the mid and upper levels the majority of the polar lows have a cold-core structure in both the 'begin' and 'mature' stage.

The phase-space for the polar lows in their 'mature' stage is presented in figure 14. The phase-space at low levels reveals that the warmest cores correspond to the more symmetric polar lows. At mid-levels there is a strong relationship between the thermal asymmetry and the core parameter, with a stronger asymmetry corellating with a colder core.

To study the changes in structure from the 'begin' stage to the 'mature' stage we calculate the changes in the two structure parameters. In figure 15 the changes in structure parameters for the low and mid-levels are plotted. At low levels the majority of the polar lows has a warming core from the 'begin' towards the 'mature' stage. The changes in thermal asymmetry are limited. At mid-levels a warming of the core correllates with a negative change in thermal asymmetry (from forward shear towards symmetric, or from symmetric towards reverse shear). When we compare these changes in structure over the polar low's lifecycle with the variability between different polar lows (figure 14) it becomes clear that the change in structure for a polar low during its intensification stage (from 'begin' to 'mature') has the same order of magnitude as the variability between the different polar lows.

The further analysis will be based on the polar lows in their mature stage. By calculating mean values of relative vorticity and pressure tendancies we can investigate the relation between polar low structure and polar low intensity and intensification. In figure 16 we find that, given a certain thermal asymmetry, the warmer the core, the more intense the cyclone. Mean values of vorticity for cold cores are $\sim$2.0 x 10^{-4} s^{-1}, while for warm cores values increase to $\sim$2.7 x 10^{-4} s^{-1}. For the intensification as measured by the six-hour pressure tendancies we find a similar relation with the strongest pressure drops (-2 hPa per 6 hours) for the warmest cores.

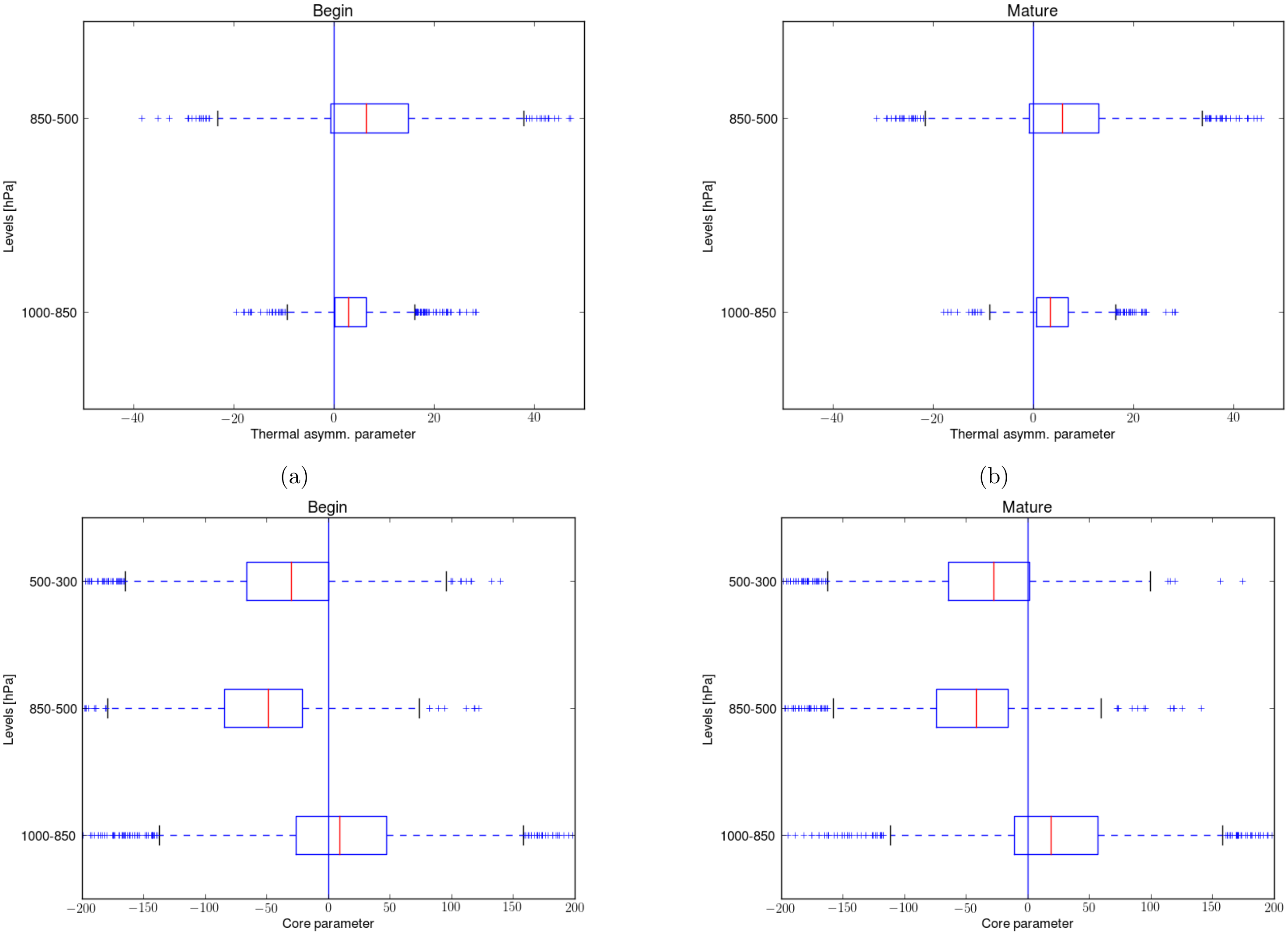

(a) (b)

(c) (d)

Figure 13: Box-and-whisker plots for the two structure parameters with different height levels at the vertical axes. The blue box is bounded by the first and third quantile of the distribution (so 50% of the values are found in this range), the red line is the median value, outliers are denoted by stars. Top figures show the thermal asymmetry parameter and bottom figures show the thermal core parameter for the begin (left) and mature stage (right).

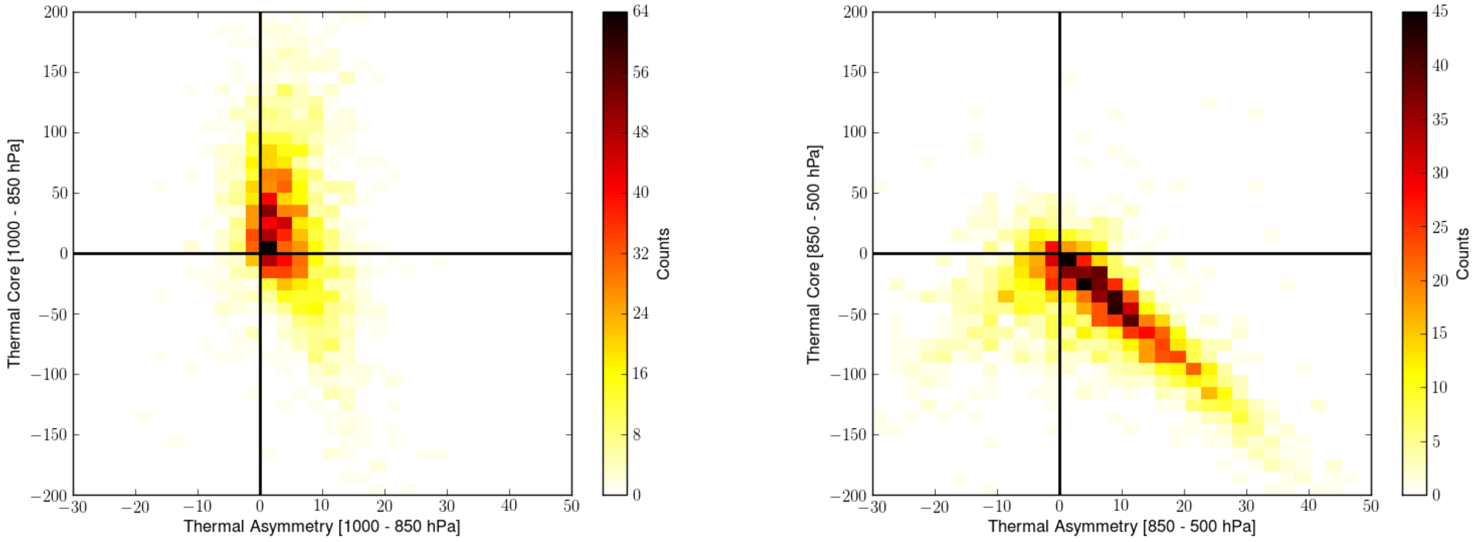

(a)

(b)

Figure 14: Phase-space for the mature stage of the polar low at low-levels (left) and mid-levels (right). The colors correspond to the counts per bin. Positive (negative) values of the core parameter indicate a warm (cold) core. Near-zero values of thermal asymmetry correspond to a symmetric polar low, negative (positive) values correspond to a reverse (normal) shear environment of the polar low.

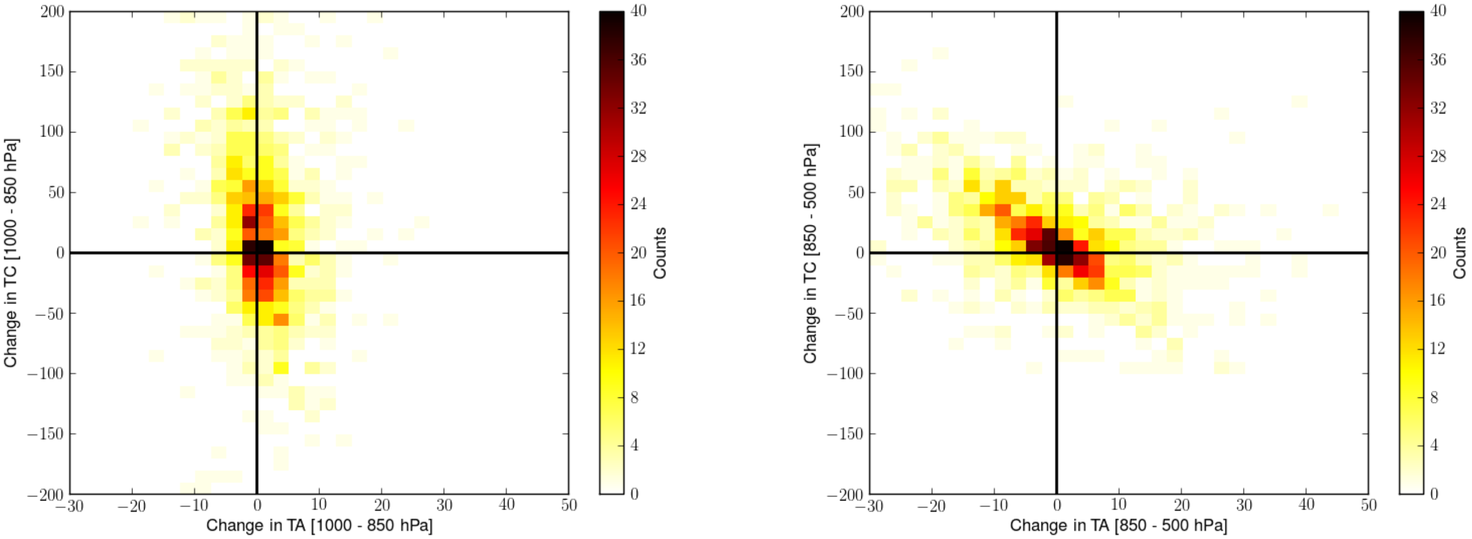

(a) (b)

Figure 15: Same as figure 14, but know for the *change* of the thermal asymmetry (TA) parameter and thermal core (TC) parameter between the 'begin' and 'mature' stage of the polar low. Positive (negative) values on the vertical axis correspond to a warming (cooling) of the core. Positive (negative) values on the horizontal axis correspond to an increase (decrease) of the thermal asymmetry parameter over time.

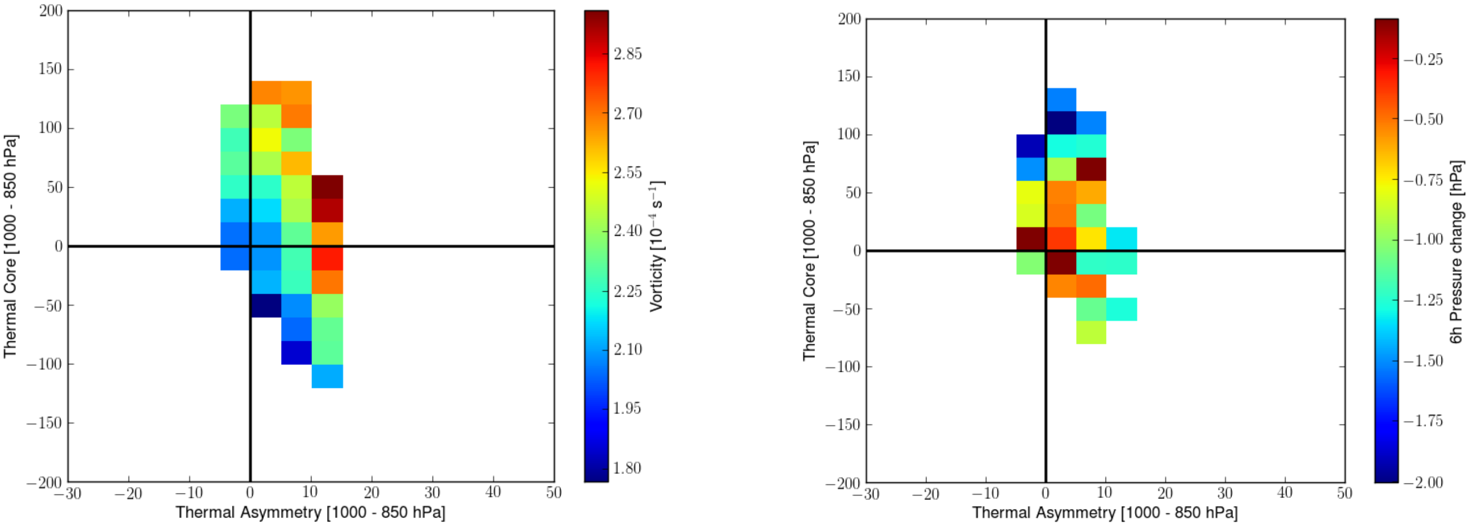

(a)

(b)

Figure 16: Mean values of relative vorticity at 10m (left) and 6 hour pressure change (right) for the mature stage in the phase-space. Mean values are only plotted if there are more than 20 counts within the bin. The pressure change is calculated over the 6h preceding the mature stage.

6.3 Forcing

The relation between thermal structure and strength of the surface heat fluxes is shown in figure 17 where the mean values of surface heat fluxes have been plotted for each bin in the phase-space. There is a clear relation between the thermal core parameter and the mean values of the surface heat fluxes. The warmest core polar lows have mean values of surface fluxes which are about 70% higher than the cold core values.

To study differences in strength and forcing parameters of the polar lows over the North Atlantic, relative fraction plots are presented. The relative fraction is defined as the fraction of polar lows within 200 km of a gridpoint exceeding the median value for a certain parameter of the complete set of 2109 polar lows. For example, for the total surface heat flux, a relative fraction of 0.5 means that exactly half the polar lows within 200 km of that gridpoint have a surface heat flux larger than 127 W m^{-2}, which is the median value for surface heat flux of all the mature polar lows.

For the vorticity the median value of all the polar lows is 2.15 x 10^{-4} s^{-1} (the threshold value for selecting the polar lows is 1.35 x 10^{-4} s^{-1}). The fraction plot shows small-scale variations of the polar low intensity over the domain.

The relative fraction of the total surface heat flux shows a maximum in the northeastern Norwegian Sea and Barents Sea. The latent heat flux increases when going southwards within in the domain whereas the sensible heat flux increases to the north of the domain (see figure 19 in the Appendix). The maximum also coincides with a region of high polar low activity as can be seen in figure 11. For the low-level baroclinicity there is a very strong north south gradient with more than 90% exceeding the median in the northern Norwegian Sea and Barents Sea and only 10-20% exceeding the median in the southern Norwegian Sea, the North Sea and the Atlantic Ocean. To the south of Iceland there is another region with a larger fraction of polar lows with a strong low-level baroclinicity.

The results for the vertical instability are presented in figure 20. The instability up to the 700 hPa level has been analysed using two different lower boundaries. The air-sea instability is measured by the difference between the 700 hPa wetbulb potential temperature and the sea surface temperature. We selected the polar lows on a threshold value of -2.8 K for this parameter. The air instability uses the 925 hPa wetbulb potential temperature as a lower boundary. Note that higher values of the instability parameters correspond to more stable conditions, thus the blue colours highlight the regions where polar lows are characterized by relatively unstable conditions. For the air-sea instability we find the most unstable conditions in the northeastern Norwegian Sea and Barents Sea, coinciding approximately with the region of highest surface fluxes. In terms of air instability the pattern is reversed, with the polar lows in the northern regions characterized by more stable conditions.

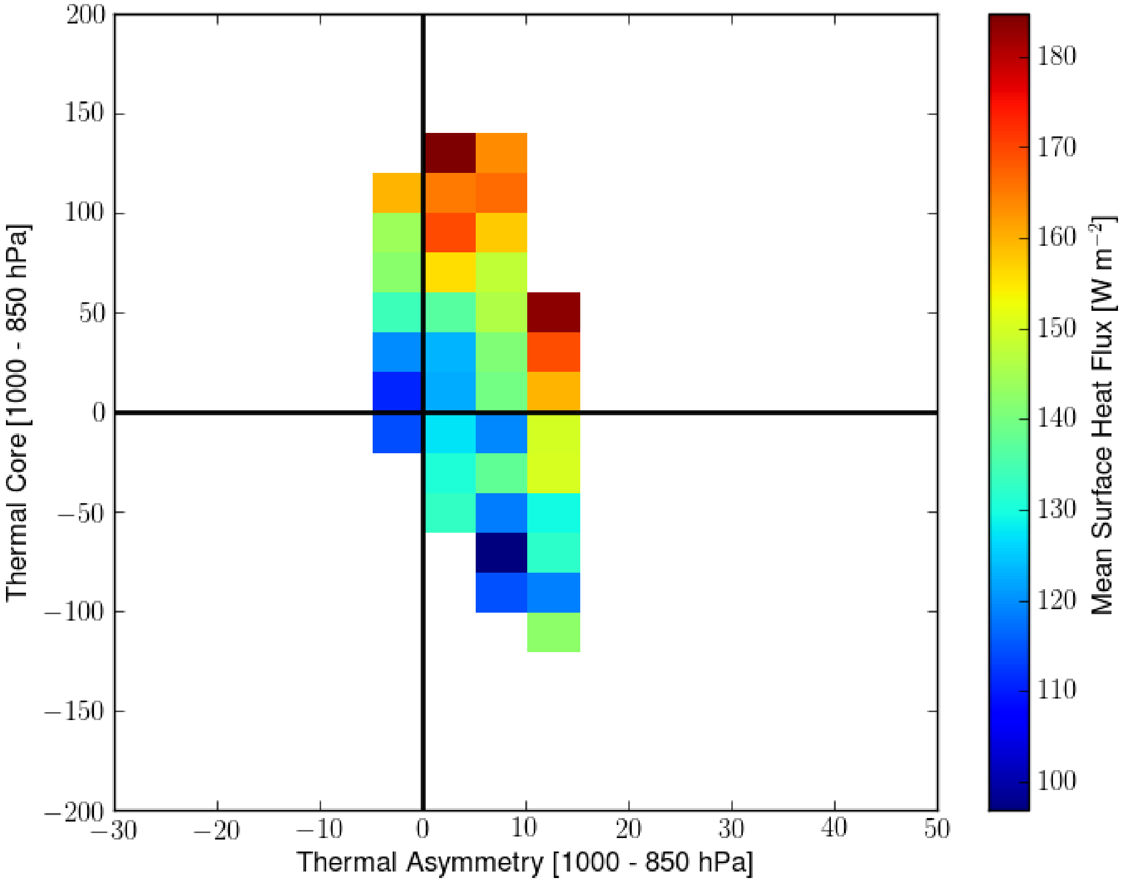

Figure 17: Mean values of surface heat flux for the mature stage in the phase-space. Mean values are only plotted if there are more than 20 counts within the bin.

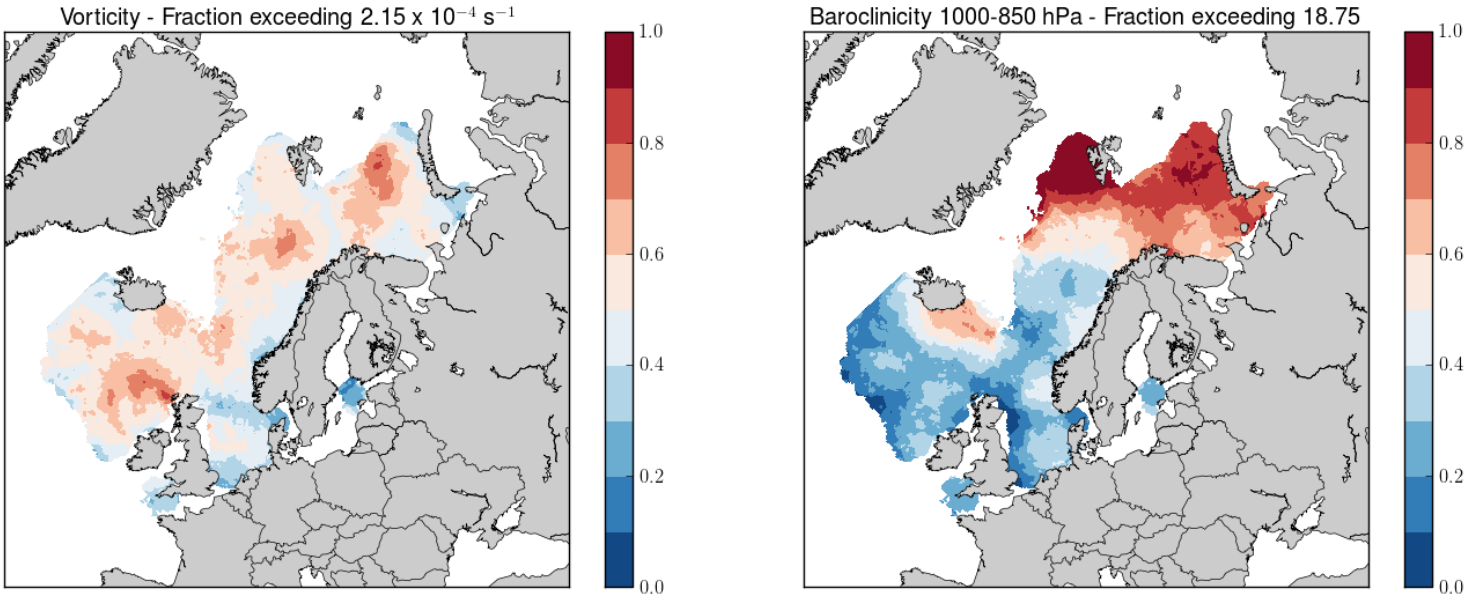

(a)

(b)

Figure 18: Relative fraction of mature polar lows within 200 km of each gridpoint exceeding median values of (a) vorticity and (b) low-level baroclinicity.

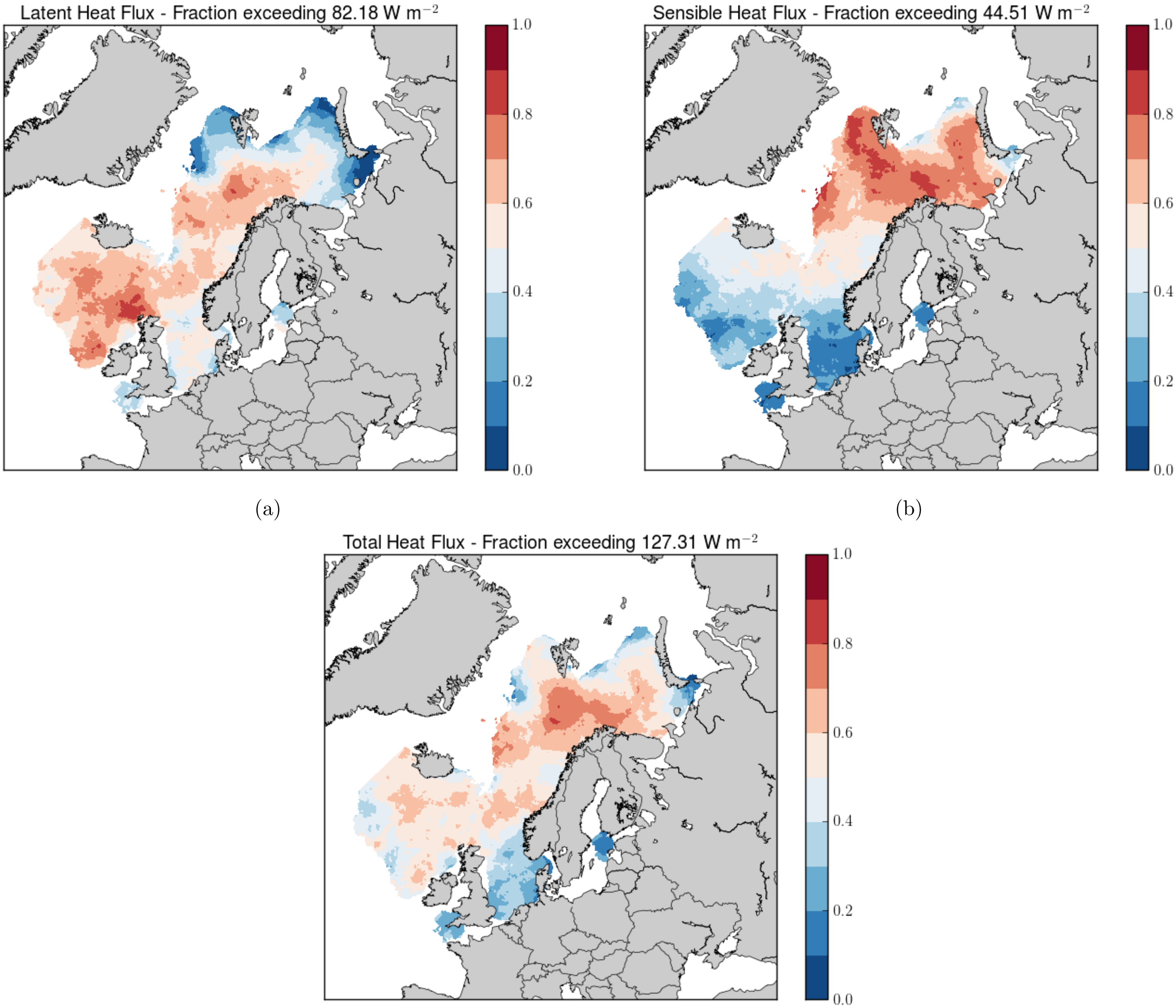

(a)

(b)

(c) Relative fraction of mature polar lows within 200 km of each gridpoint exceeding median values of (a) surface latent heat flux, (b) surface sensible heat flux and (c) total surface heat flux.

Figure 19

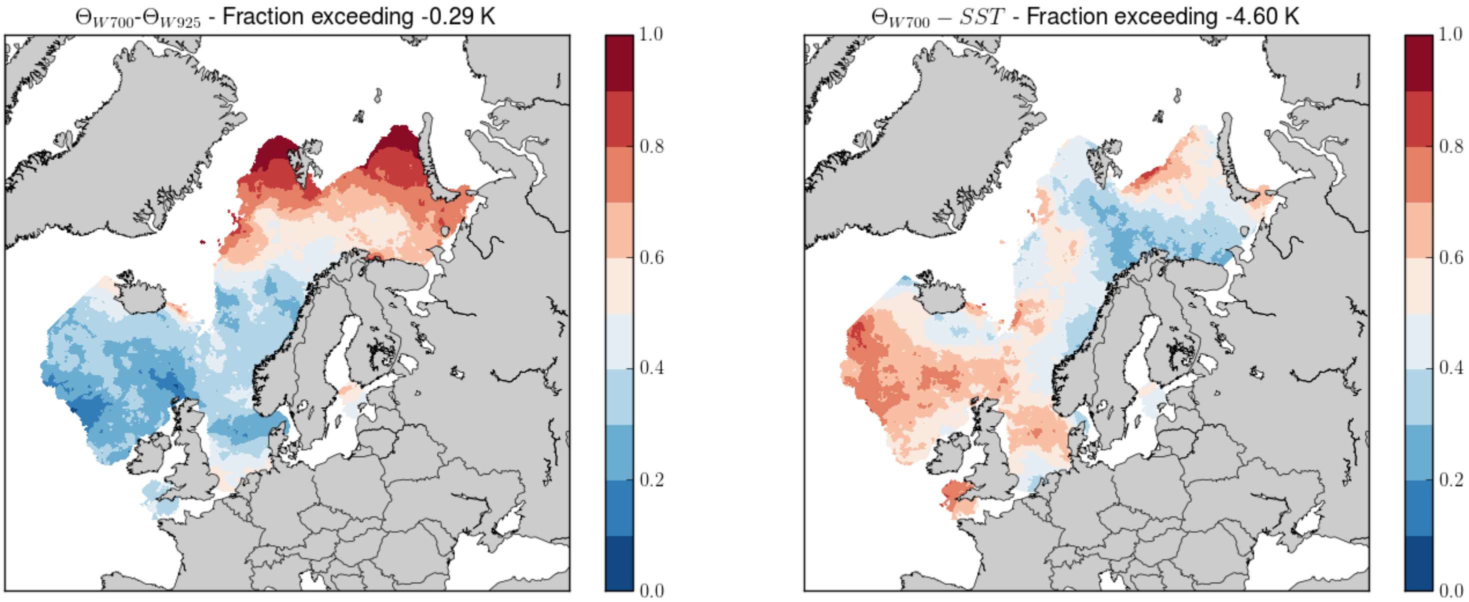

(a)

(b)

Figure 20: Relative fraction of mature polar lows within 200 km of each gridpoint exceeding median values of vertical instability as measured by the difference between (a) the 700 hPa wetbulb potential temperature and the 925 hPa wetbulb potential temperature and (b) the 700 hPa wetbulb potential temperature and the sea surface temperature. Note that for instability, the blue values correspond to a larger number of relatively unstable conditions.

7 Discussion

Climatology As mentioned in section 2.2 a few climatologies of polar lows in the North Atlantic have been constructed. In this paragraph the climatology we find is compared to earlier climatologies. We find a maximum polar low frequency of about 2.5 per year in the eastern Norwegian Sea, this is very well in agreement with the results of Bracegirdle and Gray (2008) who find a maximum spot with about 12 polar low counts over a period of 5 years. Although the identification method is the same, there are major differences between their study and this study. They do not use a tracking algorithm, which means that there is the possibility of multiple counting of the same polar low. Also, the timestep of their data is 12 hours.
The use of a tracking algorithm made it possible to identify polar low genesis regions by calculating densities from the 'begin' stage for each polar low. One of the 'genesis' regions of the polar lows is located in the eastern Norwegian Sea, near Tromsø. The polar low tracks over 4 years as found by Wilhelmsen (1985) and shown in figure 1a also show this region. When comparing the 'genesis' regions with the 'mature' stage density, we find that in the 'mature' stage the maximum is stretched over a much larger region along the Norwegian coast. Combining this with the tracks as found by Wilhelmsen (1985) it seems that many polar lows indeed form near Tromsøand travel from here southward along the Norwegian coast where they reach their maximum intensity.
The longest climatology that can be found in literature is the one by Zahn and von Storch (2008). They use a dynamical downscaling of the NCEP reanalysis dataset and apply a tracking algorithm on the polar lows. They identify polar lows by putting a threshold on minima in bandpass-filtered mean sea-level pressure. Thus they do use a size-threshold on polar low selection. The domain used by Zahn and von Storch (2008) stretches out much further to the west than our domain, it includes the Labrador Sea which has a high polar low frequency. They find about 56 polar lows per year over the full domain. In terms of geographical variations of polar low density there are some remarkable differences between Zahn and von Storch (2008) and our study. Figure 1b shows the density as calculated from the first points of each track, so we should compare this figure to the 'genesis' regions of our study (figure 11a) which was also created from the first point along the polar low track. The maximum to the south of Iceland is at a similar location, whereas the maximum in the eastern Norwegian sea is located further to the west in the study by Zahn and von Storch (2008) than in our study.
It is impossible to tell whether the differences in term of total counts as well as the location of the maxima between Zahn and von Storch (2008) and our study arise from the different datasets, the different methodologies used, or a combination of both. This would be an interesting future investigation. Xia et al. (2012) compared two identification methods, both using a different type of digital filter on the mean sea-level pressure, it would be interesting to include the method that we used and was developed by Bracegirdle and Gray (2008) in this comparison, since this method does not include a threshold on cyclone size.
Although we did not verify the tracking algorithm and subsequent polar low identification to a large database of polar low, it was shown that they succesfully captured two different polar low cases. Bracegirdle and Gray (2008) found the procedure to be successful in the Nordic Seas, with only a limited amount of false detections. In our study we find some polar low detections during the summer seasons, occurring mainly outside the Nordic Seas in the more southern parts of the domain (see figures 22 and 23 in the Appendix). A visual inspection of some individual cases showed that these detections are related to upper-level cut-off lows. Apparently the surface circulation of these vortices is strong enough to be detected as a polar low. This suggests that the objective polar low identification method of Bracegirdle and Gray (2008) has to be adapted for use outside the Nordic Seas. Since the upper-level cut-off lows are larger in scale than the polar lows, using a threshold on cyclone size, will probably be helpful. In addition it would be useful to study the relation between the relative vorticity and the 10m wind speeds. This would allow for a more careful determination of the vorticity threshold. Since the total number of counts in the summer months accounts for only 5% of all the polar lows, these systems are of limited influence on the results in terms of climatology, structure and forcing.
Several authors (e.g. Wilhelmsen (1985) and Lystad (1986) found that the number of polar low counts

in the Norwegian Sea reaches a minimum in February when compared to January and March. However, these analyses were over a rather short period including only a few winters. For the long-time monthly climatology as presented in figure 12 we do not find this February nadir. An interesting future investigation would be to relate polar low counts to large-scale circulation patterns. Claud et al. (2007) analysed the relation between the NAO and conditions which are assumed to be favourable for polar low formation. The long term polar low climatology constructed in this study allows to relate regional polar low activity directly to large-scale circulation patterns.

Structure In this study we applied the phase-space developed by Hart (2003) to study (extra-)tropical cyclones on polar lows to capture their thermal structure in terms of the thermal asymmetry and warm- or cold-core structure. The results show that the majority (70%) of the polar lows is characterized by a warm core at low levels and a forward shear environment with the thermal wind in the same direction as the movement of the polar low.

The occurrence of a warm core in most polar lows is in agreement with the similarity between polar lows and tropical cyclones as noted by several authors before (e.g. Emanuel and Rotunno (1989), Nordeng and Rasmussen (1992)). The changes from the 'begin' stage to the 'mature' stage show that a significant number of polar lows has both a cold core and warm core structure during their lifecycle. This hints at the different processes (baroclinicity, upper-level disturbances, surface fluxes, latent heat release in deep convection) contributing to the polar low intensification. Hart (2003) finds a similar result for extra-tropical cyclones with large changes of structure over the life-cycle.

Whereas at low levels most polar lows have a warm core, at mid-levels (850-500 hPa), a cold core structure dominates (80%). This shows that polar lows are rather shallow systems when compared to tropical cyclones where the warm core structure often extents to the 400 hPa level (Stern and Nolan (2011)).

It is shown that the majority of polar lows (70%) is characterized by positive values of thermal asymmetry and thus correspond to forward shear conditions in which the polar low motion is in the same direction as the thermal wind with the warm air to the right. Duncan (1978) showed that reverse-shear conditions are favourable for polar low development. Several authors performed case-studies on reverse-shear polar lows (e.g. Reed and Duncan (1987), Grø nås and Kvamstø (1995)) but no climatological investigations have been done before.

The phase-spaces at low and mid-levels reveal the wide spectrum of polar lows in terms of thermal structure. For the low-level phase-space we find that the maximum frequency of more symmetric systems is aligned vertically. This argues that the development of a warm core structure is related to non-frontal processes. At the mid-levels we find a strong relation between the core structure and the thermal asymmetry with higher values of thermal asymmetry correlating with a colder core. The changes in phase-space between the 'begin' and 'mature' stage of each polar low confirm that the warming of the core is not related to changes in low-level asymmetry. At mid-levels this pattern is rather different with a negative change in thermal asymmetry correlating with a warming of the core at this level. Note that most polar lows are characterized by a cold-core at the mid-levels, thus a warming of the mid-level core should be interpreted as a decrease in mid-level cold core strength. The warmest core cyclones are found to be most intense in terms of relative vorticity, Hart (2003) found a similar relation for his analysis on (extra-)tropical cyclones. For the intensification rate - as measured by the 6 hour pressure tendancy - we find that the warmest core cyclones show the strongest intensification. These results are in agreement with earlier studies (e.g. Delden (1989) and Emanuel and Rotunno (1989)).

Forcing Our results show that the warmest core cyclones have values of total surface heat flux which are about 70% higher than the colder core cyclones independent of the thermal asymmetry. For the polar lows having a thermal core parameter close to zero we find increasing values of the mean surface heat flux with increasing thermal asymmetry. Through thermal wind balance, a warm-core structure implies that the strongest vortex is found at the surface, which can explain the large values of the surface heat fluxes through a stronger air-sea interaction. One could also argue that apparently the large surface heat fluxes cause a warm-core structure. In the current framework it is not possible to distinguish between cause and effect. Also there are two more candidates which can explain the occurrence of a warm-core in a cyclone: latent heat release in moist convection and warm air from the environment being trapped in the cyclone core (warm seclusion).

We investigated the geographical variation of surface heat fluxes, baroclinicity and vertical instability by comparing the local fraction exceeding the median value of the parameter for the whole dataset. It is shown that polar lows occurring in the northeastern Norwegian Sea and Barents Sea have the strongest surface heat fluxes. For the baroclinicity at the low levels associated with the polar lows we find a very strong north-south gradient, with a dominant role for baroclinicity in the northern Norwegian Sea and Barents Sea and also to the southeast of Iceland. Most probably in this region, the dominant type of polar lows is the Arctic front type as defined by Businger and Reed (1989). Arctic fronts develop due to differential heating of boundary layer air over open water and over (snow covered) sea ice or land. The front seperates unmodified from modified boundary layer air.

Bracegirdle and Gray (2008) also investigates the role of baroclinicity, by analysing the gradient in potential temperature across the baroclinic zone adjacent to the polar low. They find a similar result. For vertical instability of the air, our results also agree with Bracegirdle and Gray (2008), with more stable conditions in the northern regions, and gradually decreasing stability when going southward. In addition we find that the instability when taking the sea surface temperatures as a lower boundary, is strongest in the northeastern Norwegian Sea and Barents Sea, corresponding approximately with the region of highest surface fluxes. A possible explanation for the higher atmospheric stability in the northern parts of the domain is that these regions are close to the ice sheets, although surface fluxes can be large, it takes some time for the heat and moisture to be transported upwards, which implies that the boundary layer is rather shallow in these regions. More to the south the longer fetch of the air over sea has modified the boundary layer, up to at least the 925 hPa level leading to a larger atmospheric instability.

8 Conclusion and outlook

An objective polar low climatology for the North Atlantic region has been constructed by tracking strong cyclones occurring during marine cold-air outbreaks for the period 1970-2012. Maximum polar low frequencies are found in a region to the south of Iceland and in the eastern Norwegian Sea and Barents Sea with values of approximately 2-2.5 polar lows per year within a radius of 200 km. The climatology in terms of polar low frequency and spatial distribution is in agreement with the limited amount of subjective and objective polar low climatologies that are available over the region. For future investigations it would be interesting to compare the identification method used in this study to a method including a threshold on cyclone size on the same dataset.

By analyzing the polar lows in a thermal phase-space we find that 70% of the polar lows are characterized by a shallow warm-core extending from the surface to about 850 hPa. Also it is shown that most (70%) polar lows occur in a normal shear environment. Both the intensity and intensification rate of the polar lows increase for polar lows with a warmer core. This is consistent with existing theories on polar low intensification.

Polar lows occurring in the northern Norwegian Sea, Barents Sea and to the south-east of Iceland are characterized by large values of low-level baroclinicity. The strongest surface fluxes and vertical instability in terms of air-sea contrast are found in the eastern Norwegian Sea and Barents Sea.

In this study we have shown the potential for the thermal phase-space in characterizing the wide spectrum of polar lows in terms of their thermal structure and relating this structure to forcing parameters. In the current framework, it is hard to distinguish between cause and effect. For a more complete analysis, it is necessary to (1) carefully define the different life-stages (2) include parameters for latent heat release and upper-level disturbances. Both of these parameters could be studied by means of potential vorticity.

Acknowledgements

I would like to thank my supervisor Thomas Spengler for facilitating my stay at the Geophysical Institute at the University of Bergen and for his help and motivating words when struggling through the technical part of my thesis work. Many thanks to Annick Terpstra for the interesting discussions we had about polar lows and other topics. Thanks to Lukas Papritz for his help with the transformation of the grid coordinates and the interesting discussions during his stay in Bergen. I further appreciated the comments on the manuscript provided by Aarnout van Delden, Thomas Spengler and Annick Terpstra.

References

A Arakawa and WH Schubert. Interaction of a cumulus cloud ensemble with the large-scale environment, Part I. *Journal of the Atmospheric ...*, 1974.

TJ Bracegirdle and SL Gray. An objective climatology of the dynamical forcing of polar lows in the Nordic seas. 1919(February):1903–1919, 2008. doi: 10.1002/joc.

S Businger and RJ Reed. Cyclogenesis in cold air masses. *Weather and forecasting*, 1989.

JG Charney and A Eliassen. On the growth of the hurricane depression. *Journal of the Atmospheric Sciences*, 1964.

Chantal Claud, Bertrand Duchiron, and Pascal Terray. Associations between large-scale atmospheric circulation and polar low developments over the North Atlantic during winter. *Journal of Geophysical Research: Atmospheres*, 112, 2007. ISSN 2156-2202. doi: 10.1029/2006JD008251.

A Condron, GR Bigg, and IA Renfrew. Polar mesoscale cyclones in the northeast Atlantic: Comparing climatologies from ERA-40 and satellite imagery. *Monthly weather review*, 2006.

GC Craig and SL Gray. CISK or WISHE as the mechanism for tropical cyclone intensification. *Journal of the atmospheric sciences*, 1996.

A Van Delden. On the deepening and filling of balanced cyclones by diabatic heating. *Meteorology and Atmospheric Physics*, 145:127–145, 1989.

ACL Deveson, KA Browning, and TD Hewson. A classification of FASTEX cyclones using a heightattributable quasigeostrophic verticalmotion diagnostic. *Quarterly Journal of the ...*, 128:93–117, 2002.

CN Duncan. A numerical investigation of polar lows. *Quarterly Journal of the Royal Meteorological Society*, 103:255–267, 1977.

CN Duncan. Baroclinic instability in a reversed shear flow. *Met. Mag.(Lond.)*, 107:17–23, 1978.

KA Emanuel. An air-sea interaction theory for tropical cyclones. Part I: Steady-state maintenance. *Journal of the Atmospheric Sciences*, 1986.

Kerry a. Emanuel and Richard Rotunno. Polar lows as arctic hurricanes. *Tellus A*, 41A(1):1–17, January 1989. ISSN 02806495. doi: 10.1111/j.1600-0870.1989.tb00362.x.

S Grø nås and NG Kvamstø. Numerical simulations of the synoptic conditions and development of Arctic outbreak polar lows. *Tellus A*, 47(A):797–814, 1995.

D G Harley. Frontal contour analysis of a polar low. *Meteorol. Mag*, 89:146–147, 1960.

T W Harrold and K A Browning. The polar low as a baroclinic disturbance. *Quarterly Journal of the Royal Meteorological Society*, 95(406):710–723, 1969.

RE Hart. A Cyclone Phase Space Derived from Thermal Wind and Thermal Asymmetry. *Monthly Weather Review*, 131(4):585–616, April 2003. ISSN 0027-0644. doi: 10.1175/1520-0493(2003)131¡0585:ACPSDF¿2.0.CO;2.

KI Hodges. A general method for tracking analysis and its application to meteorological data. *Monthly Weather Review*, 1994.

XY Huang and X Yang. A new implementation of digital filtering initialization schemes for HIRLAM. Technical report, 2002.

EW Kolstad. A new climatology of favourable conditions for reverseshear polar lows. *Tellus A*, (344): 344–354, 2006.

JE Kristjánsson, I Barstad, T Aspelien, I Fø re, Ø Godø y, Ø Hov, E Irvine, T Iversen, E Kolstad, TE Nordeng, H McInnes, R Randriamampianina, J Reuder, Ø Saetra, M Shapiro, T Spengler, and H Ólafsson. The Norwegian IPYTHORPEX: Polar Lows and Arctic Fronts during the 2008 Andøya Campaign. *Bulletin of the American Meteorological Society*, 92(11):1443–1466, November 2011. ISSN 0003-0007.

T Linders and Ø Saetra. Can CAPE Maintain Polar Lows? *Journal of the Atmospheric Sciences*, 67(8): 2559–2571, August 2010. ISSN 0022-4928. doi: 10.1175/2010JAS3131.1.

I T Lyall. The polar low over Britain. *Weather*, 27(9):378–390, 1972.

M Lystad. Polar lows in the Norwegian, Greenland and Barents Sea. *Final Rep., Polar Lows Project, The Norwegian Meterological Institute*, page 196, 1986.

DA Mansfield. Polar lows: The development of baroclinic disturbances in cold air outbreaks. *Quarterly Journal of the Royal Meteorological Society*, 100(426):541–554, 1974.

RJ Murray and I Simmonds. A numerical scheme for tracking cyclone centres from digital data Part I: development and operation of the scheme, 1991.

M Muskulus and D Jacob. Tracking cyclones in regional model data: the future of Mediterranean storms. *Advances in Geosciences*, pages 13–19, 2005.

Urs Neu, Mirseid G Akperov, Nina Bellenbaum, Rasmus Benestad, Richard Blender, Rodrigo Caballero, Angela Cocozza, Helen F Dacre, Yang Feng, Klaus Fraedrich, Jens Grieger, Sergey Gulev, John Hanley, Tim Hewson, Masaru Inatsu, Kevin Keay, Sarah F Kew, Ina Kindem, Gregor C Leckebusch, Margarida L R Liberato, Piero Lionello, Igor I Mokhov, Joaquim G Pinto, Christoph C Raible, Marco Reale, Irina Rudeva, Mareike Schuster, Ian Simmonds, Mark Sinclair, Michael Sprenger, Natalia D Tilinina, Isabel F Trigo, Sven Ulbrich, Uwe Ulbrich, Xiaolan L Wang, and Heini Wernli. IMILAST: A Community Effort to Intercompare Extratropical Cyclone Detection and Tracking Algorithms. *Bulletin of the American Meteorological Society*, 94(4):529–547, September 2012. ISSN 0003-0007. doi: 10.1175/BAMS-D-11-00154.1.

TE Nordeng and EA Rasmussen. A most beautiful polar low. A case study of a polar low development in the Bear Island region. *Tellus A*, 44(2):81–99, 1992. ISSN 1600-0870. doi: 10.1034/j.1600-0870.1992.00001.x.

KV Ooyama. A dynamical model for the study of tropical cyclone development. *Geofis. Int*, 4:187–198, 1964.

JG Pinto and T Spangehl. Sensitivities of a cyclone detection and tracking algorithm: individual tracks and climatology. *Meteorologische ...*, 14(6):823–838, 2005. doi: 10.1127/0941-2948/2005/0068.

E Rasmussen. The polar low as an extratropical CISK disturbance. *Quarterly Journal of the Royal Meteorological Society*, 105(445):531–549, 1979. ISSN 1477-870X. doi: 10.1002/qj.49710544504.

E Rasmussen. An investigation of a polar low with a spiral cloud structure. *Journal of Atmospheric Sciences*, 1981.

EA Rasmussen and J Turner. *Polar lows: mesoscale weather systems in polar regions*. Cambridge University Press, Cambridge, 2003. ISBN 9780521624305.

RJ Reed and CN Duncan. Baroclinic instability as a mechanism for the serial development of polar lows: a case study. *Tellus A*, 1987.

M Reistad, Ø Breivik, H Haakenstad, OJ Aarnes, BR Furevik, and J-R Bidlot. A high-resolution hindcast of wind and waves for the North Sea, the Norwegian Sea, and the Barents Sea. *Journal of Geophysical Research*, 116(C5):C05019, May 2011. ISSN 0148-0227. doi: 10.1029/2010JC006402.

C Snyder and RS Lindzen. Quasi-geostrophic wave-CISK in an unbounded baroclinic shear. *Journal of the atmospheric sciences*, 1991.

Daniel P Stern and David S Nolan. On the Height of the Warm Core in Tropical Cyclones. *Journal of the Atmospheric Sciences*, 69(5):1657–1680, November 2011. ISSN 0022-4928. doi: 10.1175/JAS-D-11-010.1. URL `http://dx.doi.org/10.1175/JAS-D-11-010.1`.

U. Ulbrich, G. C. Leckebusch, and J. G. Pinto. Extra-tropical cyclones in the present and future climate: a review. *Theoretical and Applied Climatology*, 96(1-2):117–131, January 2009. ISSN 0177-798X. doi: 10.1007/s00704-008-0083-8.

P Unden, L Rontu, H Järvinen, and P Lynch. HIRLAM-5 scientific documentation. (December), 2002.

SM Uppala, PW Kå llberg, AJ Simmons, U Andrae, V Bechtold, M Fiorino, JK Gibson, J Haseler, A Hernandez, and GA Kelly. The ERA-40 re-analysis. *Quarterly Journal of the Royal Meteorological Society*, 131(612):2961–3012, 2005.

H Wernli and C Schwierz. Surface cyclones in the ERA-40 dataset (1958-2001). Part I: Novel identification method and global climatology. *Journal of the atmospheric sciences*, pages 2486–2507, 2006.

K Wilhelmsen. Climatological study of galeproducing polar lows near Norway. *Tellus A*, 1985.

L Xia, M Zahn, KI Hodges, F Feser, and H Von Storch. A comparison of two identification and tracking methods for polar lows. *Tellus A*, 64:1–11, February 2012. ISSN 1600-0870. doi: 10.3402/tellusa.v64i0.17196.

KM Xu and KA Emanuel. Is the tropical atmosphere conditionally unstable? *Monthly weather review*, 1989.

M Zahn and Hans von Storch. A long-term climatology of North Atlantic polar lows. *Geophysical Research Letters*, 35(22):L22702, November 2008. ISSN 0094-8276. doi: 10.1029/2008GL035769.

9 Appendix

9.1 Additional figures

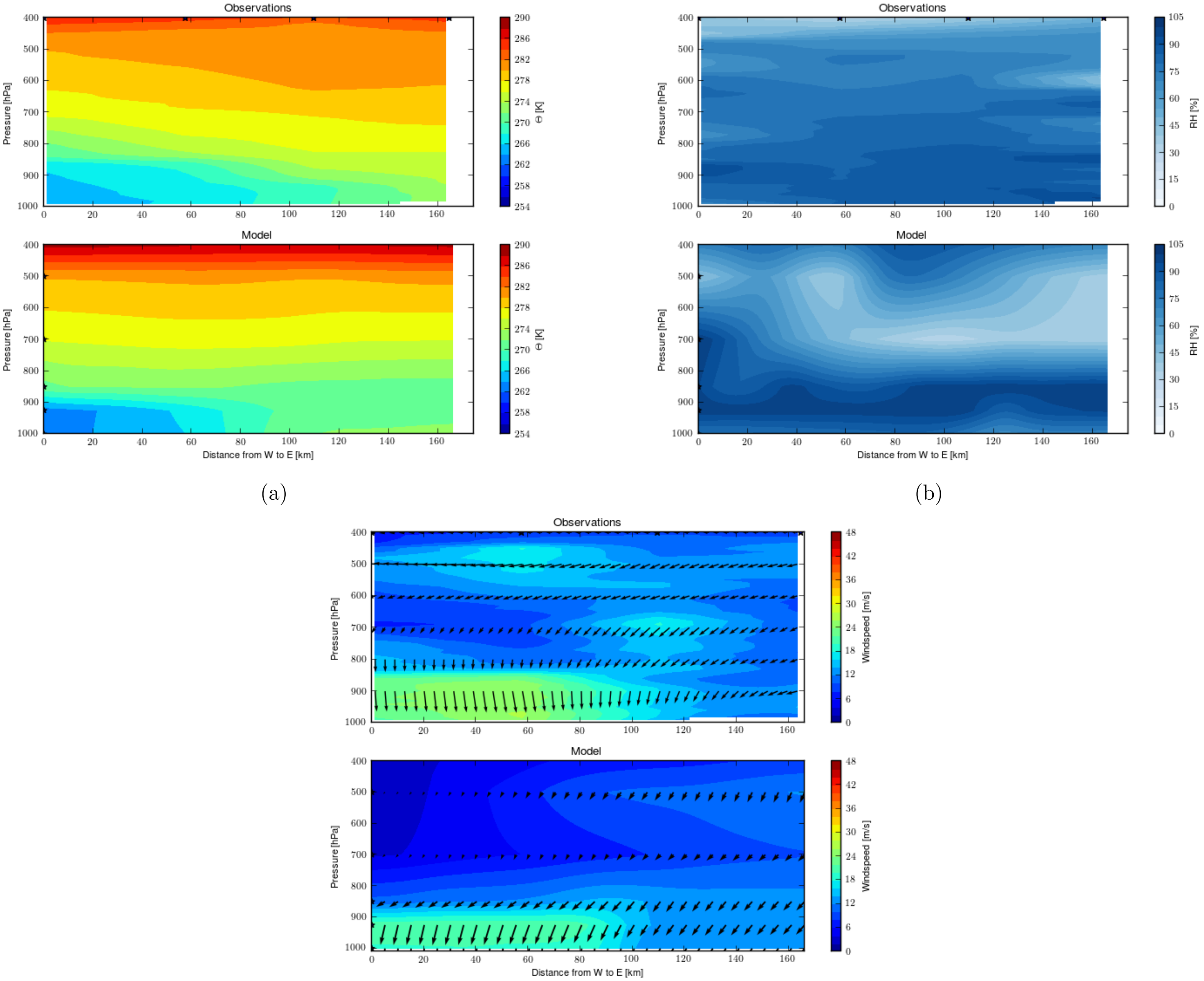

(a)

(b)

(c)

Figure 21: Crossections interpolated from dropsonde observations (top of each subfigure) and from the NORA10 model output (bottom of each subfigure) for cross-section ’B’ (see figure 3a) through the baroclinic zone. The black stars indicate dropsonde locations and model pressure levels.

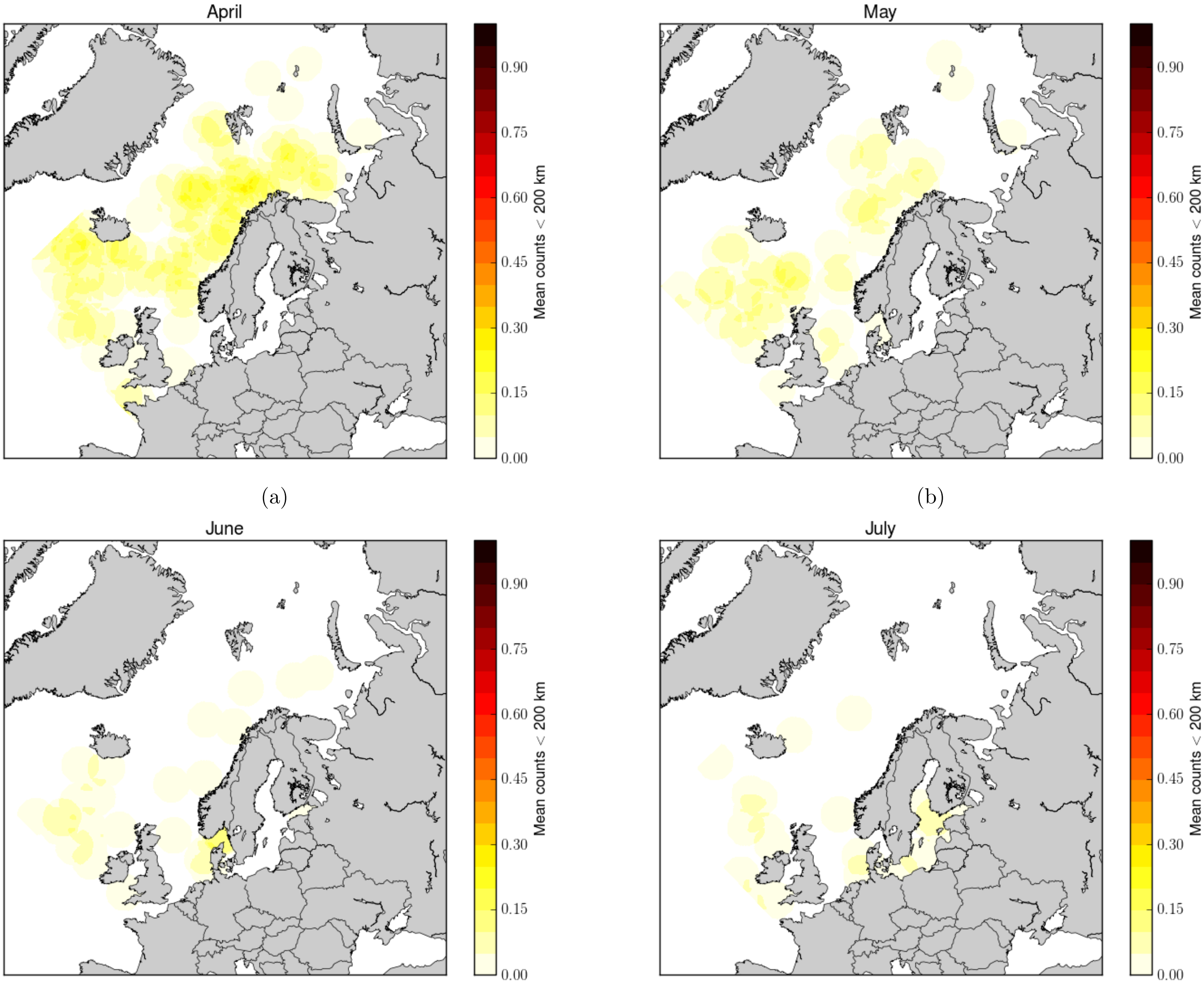

(a) (b) (c) (d)

Figure 22: Polar low frequency in counts within 200 km per month for the months (a) April, (b) May, (c) June and (d) July.

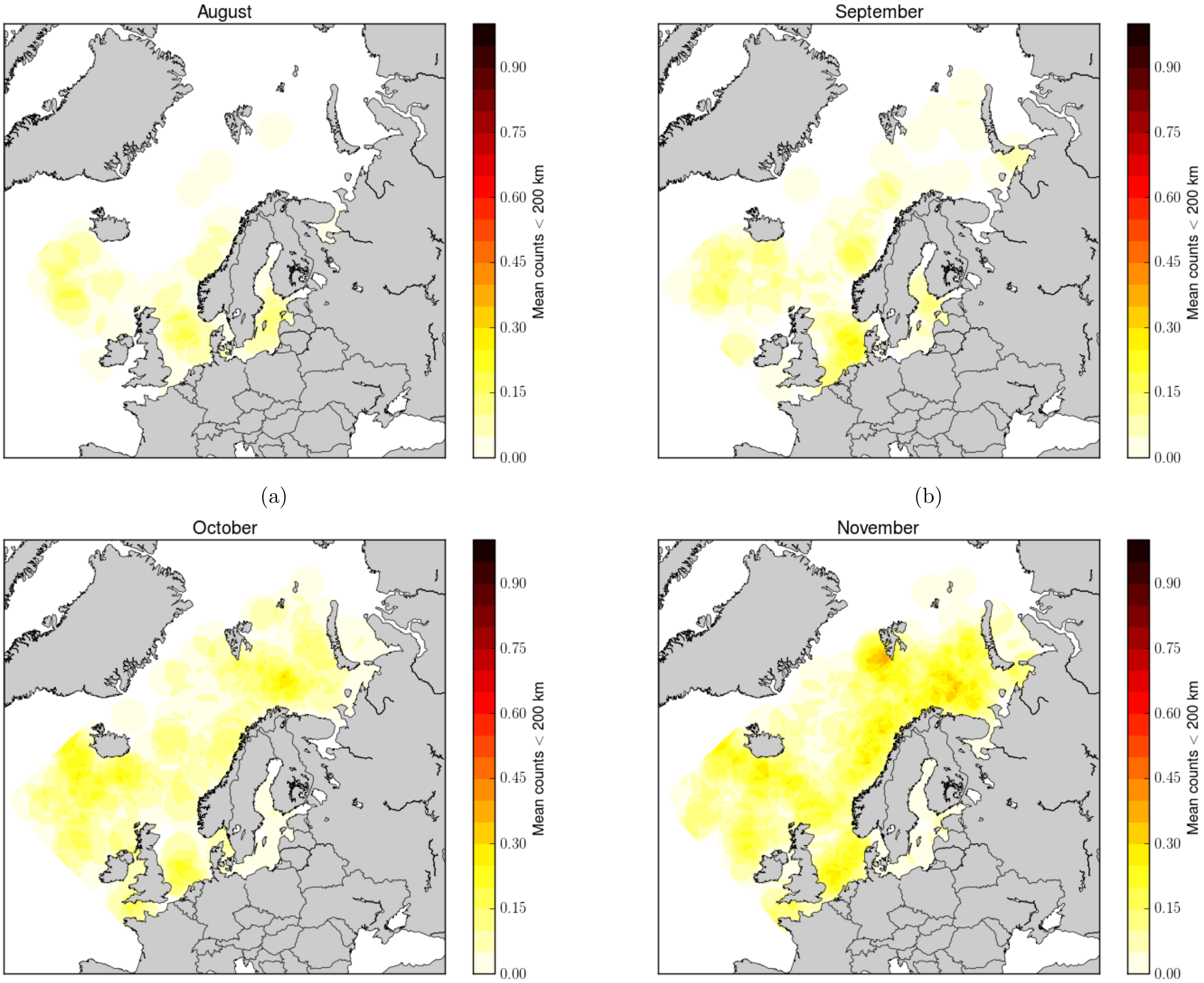

(a) (b)

(c) (d)

Figure 23: As in figure 22, but now for the months (a) August, (b) September, (c) Oktober and (d) November.

9.2 Python Code

```
#!/usr/bin/python

import numpy as np
import datetime
from Scientific.IO.NetCDF import NetCDFFile
from scipy.ndimage.filters import gaussian_filter, minimum_filter, generic_filter
from postprocessing import *
import collections as co
import itertools as it
from plotter import *
import pickle
import mettools as met
from mpl_toolkits.basemap import Basemap, maskoceans
from multiprocessing import Pool
import time
import datetime


#######################################################################################
############################# MODEL AND FEATURES ###################################
#######################################################################################

def get_model_lat_lon():
  '''
  # This function returns the 2D lat,lon arrays
  '''
  filename  = trackpars['modellatlondir']
  f         = NetCDFFile(filename,'r')
  lat       = np.array(f.variables['lat2d'])
  lon       = np.array(f.variables['lon2d'])
  return lat,lon

def get_model_field(time,fname,varname,z):
  filename  = trackpars['modeldir']+time.strftime('%Y')+fname
  f         = NetCDFFile(filename,'r')
  # Select right time
  t         = (int(time.strftime('%j'))-1)*4+int(time.strftime('%H'))/6
  if z==-1:
    field     = np.array(f.variables[varname][t,:,:])
  else:
    field     = np.array(f.variables[varname][t,z,:,:])
  f.close()
  return field

def get_features(time):
  nora.update(time)
  field_smth  = gaussian_filter(nora.field,trackpars['smooth_rad'])
  mn        = minimum_filter(field_smth,size=trackpars['filter_rad'], mode='constant')
```

```
  ii,jj     = np.nonzero(field_smth == mn)
  # Now build the features
  featurelist = []
  for n,(i,j) in enumerate(zip(ii,jj)):
    if i < nora.lat.shape[0]-trackpars['boundary'] and i > trackpars['boundary'] and j < nora.lat
    .shape[1]-trackpars['boundary'] and j > trackpars['boundary']:
      featurelist.append(minifeature(i,j,nora.lat[i,j],nora.lon[i,j],nora.field[i,j],nora.time))
  # Print some statistics
  print "Detection: found ", len(featurelist), " features at ", nora.time.strftime('%Y%m%d%H')
  return featurelist

class minimodel:
  def __init__(self):
    self.dt        = trackpars['timestep']
    self.lat,self.lon  = get_model_lat_lon()
    self.landmask = maskoceans(self.lon,self.lat,self.lat,inlands=False,resolution='i',grid=1.25)
    .mask
  def update(self,time):
    self.field     = get_model_field(time,'.pres.nc','pres',0)
    self.time      = time

class minifeature:
  def __init__(self,i,j,lat,lon,val,time):
    self.i  = i
    self.j  = j
    self.lat = lat
    self.lon = lon
    self.val = val
    self.time = time
    # Meteo
    self.tw700  = None
    self.t_skin = None
    self.vrt  = None
    self.atsea  = None
    self.pl   = None
    self.etc  = None
    # Related to tracking
    self.p  = None
    self.c    = None
    self.role = None
    self.explored   = False
    self.visited  = False
    self.group    = None
  def tracking_init(self,role):
    # Related to tracking
    self.role = role
    self.explored   = False
    self.visited  = False
    self.group    = None
```

```
def get_meteo(featuregroup):
  for f in featuregroup:
    try:
      # We need RH700, T700, tskin
      rh700 = get_model_field(f.time,'.700.r.nc','r',0)[f.i,f.j]
      pt700 = get_model_field(f.time,'.700.pt.nc','pt',0)[f.i,f.j]
      t_skin = get_model_field(f.time,'.t.nc','t',-1)[f.i,f.j]
      t700 = pt700*(700./1000.)**0.286
      td = met.calc_td(t700,rh700)
      theta_w700 = met.OW(td,t700,700.)
      # Now add it to feature
      f.tw700 = theta_w700
      f.t_skin = t_skin
      f.vrt = get_local_vorticity(nora,f,trackpars['vrt_radius'])
      f.atsea = nora.landmask[f.i,f.j]
      f.pl  = (f.tw700-f.t_skin) < trackpars['temp_thres'] and f.vrt >= trackpars['vrt_thres']
    and f.atsea
      f.etc = (f.tw700-f.t_skin) >=trackpars['temp_thres'] and f.vrt >= trackpars['vrt_thres']
    and f.atsea
    except:
      print "Error getting meteo for time: ", f.time.strftime('%Y%m%d%H')
  return featuregroup

def get_cluster(queue,allfeatures,ID):
  '''
  # This function performs a depth first search to explore one connected cluster of features
  '''
  while queue:
    f1 = queue.pop()
    if not f1.explored:
      f1.explored = True
      for f2 in allfeatures:
        if not f2.visited and check_dist_thres(f1,f2) and not f1.time == f2.time:
          f2.group = ID
          f2.visited  = True
          queue.append(f2)
          get_cluster(queue,allfeatures,ID)
    else:
      pass

def cluster_features(allfeatures):
  '''
  # This function loops through all the features in a two-timestep set (parents+childs) and
    groups them based on a distance threshold
  '''
  n=0
  for f in allfeatures:
    if not f.explored: # was f.visited!!
      # Get group performs a depth-first search to find all features connected to f
      get_cluster([f],allfeatures,n)
```

```
      n=n+1
    else:
      n=n+1
      pass
  featuregroups=[]
  featuregroup_number=[]
  # Now plot the grouped features (not projected on earth)
  #plot_grouped_features(allfeatures)
  group_numbers = [f.group for f in allfeatures]
  features      = [f for f in allfeatures]
  for nr in set(group_numbers):
    featuregroups.append([f for f in features if (f.group==nr and f.group is not None)])
  return featuregroups


################################################################################
############################ GETTING SEGMENTS ##################################
################################################################################

class tracksegment:
  '''
  A tracksegment consists of a parent feature and child feature
  '''
  def __init__(self, parent, child):
    self.p          = parent  # The parent feature
    self.c          = child   # The child feature
    self.selected   = False   # After the algorithm is run, the selected segments constitute the track
    A       = (1./(2.*trackpars['dx']*trackpars['dy']))
    ds,dx,dy  = dist_km(self.p.lat,self.c.lat,self.p.lon,self.c.lon)
    self.lh   = A*np.exp(-dx**2/(2*trackpars['dx']**2)-dy**2/(2*trackpars['dy']**2))


def optimizer(parents,childs):
  '''
  # Do not return anything, just linking them
  '''
  # Set the tracking parameters (childs become parents at the next timestep! )
  for p in parents:
    p.tracking_init('p')
  for c in childs:
    c.tracking_init('c')
  # Cluster them based on distance
  clustered_features = cluster_features(parents+childs)
  # Build all allowed branches per cluster
  clustered_segments = get_segments(clustered_features)
  # Build the segments
  clustered_track = []
  for segments in clustered_segments:
    # Now we are within one cluster of segments
```

```
    combilist = [combi for combi in get_combos(segments)]
    best = get_best_combi(combilist)
    # Append it to the clustered_track only if it is not None, so from now length can differ!
    if best is not None:
      clustered_track.append(best)
  #plot_optimized(parents,childs,clustered_track)
  # Link parents and childs
  link_features(clustered_track)

def link_features(clustered_track):
  # Note difference between segment parent/child and feature parent/child!!
  for track in clustered_track:
    for s in track:
      # The child of the segment's parent becomes his child,
      # and the parent of the segment's child becomes his parent.
      s.p.c = s.c
      s.c.p = s.p

def get_best_combi(combilist):
  '''
  # Returns the best combination of segments by summing the likelihood of individual segments
  '''
  lh_max = 0
  best_combi = None
  for combi in combilist:
    lh_combi = 0
    for s in combi:
      lh_combi += s.lh
    if lh_combi > lh_max:
      lh_max = lh_combi
      best_combi = combi
  return best_combi

def check_dist_thres(p,c):
  ds,dx,dy = dist_km(p.lat,c.lat,p.lon,c.lon)
  if np.abs(dx) <= trackpars['dx'] and np.abs(dy) <= trackpars['dy']:
    return True
  else:
    return False

def get_segments(clusters):
  clustered_segments = []
  for cluster in clusters:
    # Split out to parents and childs again!
    parents = [f for f in cluster if f.role=='p']
    childs  = [f for f in cluster if f.role=='c']
    segments = []
    # Iterate over all combinations
    for p in parents:
      for c in childs:
```

```
        if check_dist_thres(p,c):
          s = tracksegment(p,c)
          segments.append(s)
    clustered_segments.append(segments)
  return clustered_segments

def unique(list_):
  return len(set(list_)) == len(list_)

def get_combos(branches):
  by_parent = co.defaultdict(list)
  for branch in branches:
    by_parent[branch.p].append(branch)
  combos = it.product(*by_parent.values())
  return it.ifilter(lambda x: unique([b.c for b in x]), combos)

##################################################################################
####################### CREATING THE TRACKS ######################################
##################################################################################


class track:
  def __init__(self,features):
    self.features = features
    self.update()
  def update(self):
    self.time     = [f.time for f in self.features]
    self.prs      = [f.val for f in self.features]
    self.lat      = [f.lat for f in self.features]
    self.lon      = [f.lon for f in self.features]

def get_stats(tracklist):
  # minimal pressure
  minprs    = [np.min(t.prs) for t in tracklist]
  # track length
  tracklength = [len(t.features) for t in tracklist]
  # distance travelled
  print "Mean tracklength   = ", np.mean(tracklength)
  print "Mean minprs    = ", np.mean(minprs)

def get_tracks(fg):
  mytracklist = []
  for f in fg:
    # If there is no parent, but there is a child, this is the start of a track
    if f.p is None and f.c is not None:
      tf = f
      # Now loop through this track
      track_features = []
      while tf.c is not None:
        track_features.append(tf)
```

```
        tf = tf.c
      mytracklist.append(track(track_features))
  return mytracklist


################################################################################
################################### METEO ######################################
################################################################################


def get_local_vorticity(nora,feature,radius):
  i = feature.i
  j = feature.j
  time = feature.time
  window = radius+1
  uwd = get_model_field(time,'.10u.nc','10u',0)
  vwd = get_model_field(time,'.10v.nc','10v',0)
  uwd = uwd[i-window:i+window+1,j-window:j+window+1]
  vwd = vwd[i-window:i+window+1,j-window:j+window+1]
  lat = nora.lat[i-window:i+window+1,j-window:j+window+1]
  lon = nora.lon[i-window:i+window+1,j-window:j+window+1]
  kernel = np.zeros_like(uwd)
  y,x = np.ogrid[-window:window+1, -window:window+1]
  mask = x**2 + y**2 <= radius**2
  kernel[mask] = 1
  vrt = calc_rel_vort(lat,lon,uwd,vwd)
  vrt_cyc = np.mean(vrt[kernel.astype(bool)])
  return vrt_cyc

################################################################################
################################### GENERAL ####################################
################################################################################

def save_object(myobject,name):
  '''
  # usage: save_object(some_object, objectname(str) )
  '''
  print "Saving ", name
  f = open(trackpars['pickledir']+trackpars['runname']+name+'.pic','w')
  pickle.dump(myobject,f)
  f.close()

def load_object(name):
  '''
  # usage:  some_object = load_object(objectname(str) )
  '''
  print "Loading ", name
  f = open(trackpars['pickledir']+trackpars['runname']+name+'.pic','r')
  myobject = pickle.load(f)
  f.close()
```

```python
  return myobject


################################################################################
#################################### MAIN ######################################
################################################################################


# trackpars contains all the parameters for a single run
trackpars = {
  'runname' : '40years_newer',#'40years_newer',#'40years_new''40years',  # 'test_density_30y'
  'subname' : '',
  'plot' : False,
  'ncores' : 32,
  'dx'      : 500,
  'dy'      : 500,
  'start'    : datetime.datetime.strptime('1970010100','%Y%m%d%H'),
  'end'      : datetime.datetime.strptime('2012010100','%Y%m%d%H'),
  'timestep'  : datetime.timedelta(hours=6),
  # Directories
  'modeldir'  : '/net/ukl-felles.uib.no/export/gfi-share/Reanalyses/Met.no/NORA10/NORA10.',
  'modellatlondir' : '/Home/siv25/scr021/PL/Data/NORA_grid.nc',
  'plotdir' : '/Home/siv25/scr021/Dropbox/Dropplots/',
  'plotdir_thesis' : '/Home/siv25/scr021/Dropbox/Dropplots/Thesis/',
  'plotdumpdir': '/Data/gfi/users/tsp065/students/scr021/Plots/',
  'pickledir': '/Data/gfi/users/tsp065/students/scr021/Pickle/',
  #
  'boundary': 5,
  'smooth_rad'  : 5,
  'filter_rad'  : 5,
  'vrt_radius'   : 5,
  # Polar low thresholds
  'temp_thres': -2.8,
  'vrt_thres_start': 0.65e-4,
  'vrt_thres': 1.3e-4,    # BG2008: 1.3e-4
  'pl_track_thres': 2,    # Number of points along track that have to satisfy PL criteria
  }
# Make the model
nora = minimodel()

if __name__=='__main__':

  # Feature extraction
  runtime     = trackpars['start']
  featurelist = []
  timelist = [trackpars['start']+i*nora.dt for i in range(60000) if (trackpars['start']+i*nora.dt < trackpars['end'])]

  # Run feature detection, using multiple cores
  print "Getting features using ", trackpars['ncores'], " cores"
```

```
  print "localtime = ", datetime.datetime.now().strftime("%Y-%m-%d %H:%M:%S")
  pool = Pool(processes=trackpars['ncores'])
  featurelist = pool.map(get_features,timelist)
  pool.close()


  # Get meteorology, using multiple cores
  print "Getting meteorology using ", trackpars['ncores'], " cores"
  print "localtime = ", datetime.datetime.now().strftime("%Y-%m-%d %H:%M:%S")
  pool = Pool(processes=trackpars['ncores'])
  featurelist = pool.map(get_meteo,featurelist)
  pool.close()
  print "Got meteorology! :-)"

  # Explode features to one long list
  features      = [f for fg in featurelist for f in fg]
  print "Selecting PLs"
  polarlows     = [f for f in features if f.pl==True]


  # Getting most likely segments
  segmentlist = []
  for i in range(len(featurelist)-1):
    if len(featurelist[i])>0:
      print "Getting most likely segments at time ", featurelist[i][0].time.strftime('%Y%m%d%H')
    optimizer(featurelist[i],featurelist[i+1])

  # Constructing tracks
  tracklist = []
  for i in range(len(featurelist)):
    if len(featurelist[i])>0:
      print "Constructing tracks at time ", featurelist[i][0].time.strftime('%Y%m%d%H')
      for t in get_tracks(featurelist[i]):
        tracklist.append(t)

  print "localtime = ", datetime.datetime.now().strftime("%Y-%m-%d %H:%M:%S")
  print "Now selecting polar low tracks"
  # Select polar low tracks
  polarlowtracklist = select_pl_tracks(trackpars,tracklist)
  # Select PLs landfalling in Netherlands
  dutchpolarlows = select_dutch(polarlowtracklist)

  # Save the most important objects!
  #save_object(tracklist,'tracklist')
  #save_object(polarlows,'polarlows')
  #save_object(polarlowtracklist,'polarlowtracklist')

  #polarlowtracklist = load_object('polarlowtracklist')

  print "localtime = ", datetime.datetime.now().strftime("%Y-%m-%d %H:%M:%S")
```

```
print "Getting extra meteorology, using ", trackpars['ncores'], " cores"
pool = Pool(processes=trackpars['ncores'])
polarlowtracklist = pool.map(get_extra_meteo,polarlowtracklist)
pool.close()
print "Got the extra meteorology! :-)"

print "localtime = ", datetime.datetime.now().strftime("%Y-%m-%d %H:%M:%S")
print "Reducing PL track by getting begin-mature-end using ", trackpars['ncores'], " cores"
pool = Pool(processes=trackpars['ncores'])
polarlowtracklist = pool.map(reduce_track,polarlowtracklist)
pool.close()
print "Reduced some stuff! :-)"

print "localtime = ", datetime.datetime.now().strftime("%Y-%m-%d %H:%M:%S")
print "Now splitting out to begin stages and mature stages"
pl_begin    = [t.begin for t in polarlowtracklist]
pl_mature   = [t.mature for t in polarlowtracklist]

print "localtime = ", datetime.datetime.now().strftime("%Y-%m-%d %H:%M:%S")
print "I found ", len(polarlows), " polarlows and ", len(pl_mature), " tracks."
pldata = [polarlows,pl_begin,pl_mature]
save_object(pldata,'pldata')

# Save PL tracks
save_object(polarlowtracklist,'polarlowtracklist')

# Also try to save the etcs
etcs          = [f for f in features if f.etc==True]
save_object(etcs[::100],'etcs')
```

./cyclonetracker.py